Dalton Transactions

ROYAL SOCIETY OF CHEMISTRY

PAPER

View Article Online
View Journal | View Issue

Cite this: *Dalton Trans.*, 2024, **53**, 11393

Towards efficient Ir(III) anticancer photodynamic therapy agents by extending π-conjugation on N^N ligands†

Juan Sanz-Villafruela, ‡[a] Cristina Bermejo-Casadesús, ‡[b] Marta Martínez-Alonso,[a] Artur Moro,[c] João C. Lima,[c] Anna Massaguer *[b] and Gustavo Espino *[a]

In this work we disclose a new family of biscyclometallated Ir(III) complexes of the general formula [Ir(C^N)$_2$(N^N)]Cl (**IrL1–IrL5**), where HC^N is 1-phenyl-β-carboline and N^N ligands (**L1–L5**) are different diimine ligands that differ from each other in the number of aromatic rings fused to the bipyridine scaffold. The photophysical properties of **IrL1–IrL5** were thoroughly studied, and theoretical calculations were performed for a deeper comprehension of the respective variations along the series. All complexes exhibited high photostability under blue light irradiation. An increase in the number of aromatic rings led to a reduction in the HOMO–LUMO band gap causing a red-shift in the absorbance bands. Although all the complexes generated singlet oxygen ($^1O_2$) in aerated aqueous solutions through a photocatalytic process, **IrL5** was by far the most efficient photosensitizer. Consequently, **IrL5** was highly active in the photocatalytic oxidation of NADH. The formation of aggregates in DMSO at a high concentration (25 mM) was confirmed using different techniques, but was proved to be negligible in the concentration range of biological experiments. Moreover, ICP-MS studies proved that the cellular uptake of **IrL2** and **IrL3** is much better relative to that of **IrL1**, **IrL4** and **IrL5**. The antiproliferative activity of **IrL1–IrL5** was investigated in the dark and under blue light irradiation against different cancer cell lines. Complexes **IrL1–IrL4** were found to be cytotoxic under dark conditions, while **IrL5** turned out to be weakly cytotoxic. Despite the low cellular uptake of **IrL5**, this derivative exhibited a high increase of cytotoxicity upon blue light irradiation resulting in photocytotoxicity indexes (PI) up to 38. **IrL1–IrL4** showed lower photocytotoxicity indexes ranging from 1.3 to 17.0. Haemolytic experiments corroborated the compatibility of our complexes with red blood cells. Confocal microscopy studies proved their accumulation in mitochondria, leading to mitochondrial membrane depolarization, and ruled out their localization in lysosomes. Overall, the mitochondria-targeted activity of **IrL5**, which inhibits considerably the viability of cancer cells upon blue light irradiation, allows us to outline this PS as a new alternative to traditional chemotherapeutic agents.

Received 8th February 2024,
Accepted 18th April 2024

DOI: 10.1039/d4dt00390j

rsc.li/dalton

1. Introduction

Photodynamic Therapy (PDT) is a clinically approved modality of oncologic therapy, based on the administration of an ideally non-toxic or weakly toxic photoactivatable drug, called the photosensitizer (PS). Next, the PS is locally activated by light irradiation to make it react with tissue O_2 and produce cytotoxic reactive oxygen species (ROS) that can destroy cancer cells. In addition, PDT can cause damage to microvasculature in the tumour region, which deprives cancer cells of nutrients, and can induce an active immune response.[1–3] Moreover, it is generally accepted that upon light irradiation, the resulting excited state of the PS (PS*) can generate ROS through two different photocatalytic mechanisms of action (MoA): (1) MoA of Type I, wherein the PS* produces ROS, such as the radical anion superoxide ($O_2^{\bullet-}$), the radicals hydroxyl ($OH^{\bullet}$) and hydroperoxyl ($HO_2^{\bullet}$) or hydrogen peroxide (H_2O_2), through electron or hydrogen transfer processes; (2) MoA of Type II, wherein the PS* transfers its excess energy to ground state cellular O_2 to produce singlet oxygen ($^1O_2$), regarded as the main cytotoxic

[a]*Universidad de Burgos, Departamento de Química, Facultad de Ciencias, Plaza Misael Bañuelos s/n, 09001 Burgos, Spain. E-mail: gespino@ubu.es*
[b]*Universitat de Girona, Departament de Biologia, Facultat de Ciències, Maria Aurelia Capmany 40, 17003 Girona, Spain. E-mail: anna.massaguer@udg.edu*
[c]*Universidade NOVA de Lisboa, LAQV-REQUIMTE, Departamento de Química, Faculdade de Ciências e Tecnologia, 2829-516 Caparica, Portugal*

†Electronic supplementary information (ESI) available. CCDC 2327779. For ESI and crystallographic data in CIF or other electronic format see DOI: https://doi.org/10.1039/d4dt00390j

‡These authors contributed equally.

mediator.[4,5] Ultimately, these ROS can react with essential biomolecules (DNA, proteins, and lipids) and inhibit vital biochemical pathways, leading to cancer cell death. An alternative photoredox catalytic MoA has been recently proposed, wherein NADH is oxidized directly by the PS*, which disrupts the mitochondrial electron transport chain.[6]

Thus, the main feature of PDT is that it exhibits a minimally invasive nature and offers precise spatiotemporal control over the cytotoxic activity of the activated PS and hence benefits from reduced side effects. Conceptually, this strategy is considerably effective, extremely selective, quick-acting, exceptionally versatile and can be applied repeatedly without the weakening and dose-limiting side effects of chemotherapy and radiotherapy.[4]

From a critical standpoint, despite its advantageous features, PDT has not reached full implementation due to some intrinsic drawbacks, and also because of some limitations of approved PDT PSs, such as tedious synthetic and purification procedures, low water solubility, tendency to undergo photobleaching, low capability for selective accumulation in the malignant *versus* healthy tissues and moderate quantum yields in the generation of ROS.[1,7–10] Therefore, it is clear that novel PSs are needed to overcome the aforementioned disadvantages.

Ir(III) biscyclometallated complexes are being studied as potential PDT agents or PSs[11–14] due to a number of salient chemical and photophysical properties, including the following: (1) modular synthesis that allows easy preparation and modification;[15] (2) a large electron spin–orbit coupling (SOC) constant for Ir that favours high intersystem crossing (ISC) efficiency and the access to triplet excited states;[16,17] (3) long-lived triplet excited states that can be quenched by O_2 to generate $^1O_2$ or alternative ROS;[18] (4) appropriate hydrophilic/lipophilic balance along with excellent cellular uptake and targeted intracellular distribution properties that can be modulated through ligand substitution; (5) emission properties through phosphorescence, involving large Stokes shifts that prevent self-quenching issues at high local concentrations and allow the development of bioimaging-guided protocols and theragnostic applications;[19,20] and (6) remarkable photostability, which enables repeated excitation terms for the application of multiple therapeutic cycles.

Moreover, different reports have shown that Ru(II) polypyridyl complexes with π-expansive ligands such as dppn exhibit either excellent phototoxicities toward cancer cells,[2,21] DNA photocleavage properties,[22] or antimicrobial PDT activity[23,24] as a result of their long excited-state lifetimes mainly contributed by ^{3}IL and the resulting enhanced ability to produce $^1O_2$. Some groups have also described Ir(III) bis-cyclometalated complexes with dppz and dppn (see the structures in Scheme 1). For instance, the group of Kam-Wing Lo has shown that the non-emissive complexes $[Ir(ppy)_2(N^N)]PF_6$ (N^N = dppz or dppn) bind to double-stranded DNA through intercalation, displaying emission enhancement.[25] Mao *et al.* reported the anticancer activity of a series of Ir(III) derivatives of the type $[Ir(C^N)_2(N^N)]PF_6$ (C^N = dfppy, N^N = dppz or dppn) that target mitochondria and intercalate into mtDNA to induce mtDNA damage.[26] In a different context, Ruiz *et al.* proved the antimicrobial activity *versus* multidrug-resistant bacterial strains of a family of Ir(III) analogues with different N^N ligands, such as phen, dpq, dppz and dppn.[27] More recently, Ruiz and Brabec groups uncovered that Ir(III) PSs bearing dppz display potent selective toxicity against cancer cells upon irradiation with blue light, through lysosomal damage and oncosis.[28] However, a systematic study of the potential application in PDT of Ir(III) bis-cyclometalated complexes with different π-extended di-imine ligands, including dppn, has not been performed so far.

Herein, we report the synthesis of a new family of Ir(III) bis-cyclometallated complexes with the general formula $[Ir(C^N)_2(N^N)]Cl$, wherein HC^N = 1-phenyl-β-carboline and N^N = bpy, phen, dpq, dppz, and dppn, with the objective of screening their ability to produce ROS efficiently, and analyse their potential use as PDT photosensitizers in cancer treatment. Besides, our contribution describes the underlying mechanism of action of these PSs. This effort allows us to gain a fundamental understanding of how the rational modification of the molecular structure of metal-based PSs can modulate their photophysical properties and therefore may impact their photoactivation behaviour and biological performance.

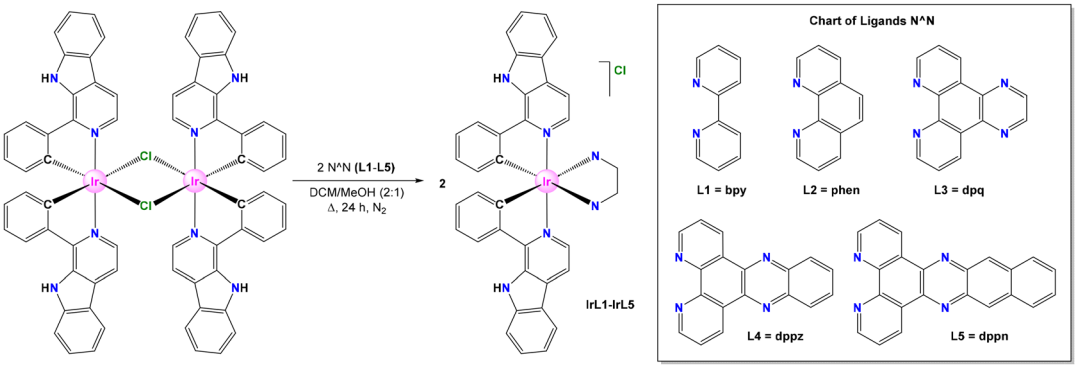

Scheme 1 Synthesis and molecular structures of the new complexes **IrL1–IrL5**.

2. Results and discussion

2.1. Synthesis of ligands and complexes

The new Ir(III) biscyclometalated complexes of the general formula *rac*-[Ir(C^N)$_2$(N^N)]Cl (HC^N = 1-phenyl-β-carboline and N^N = **L1–L5**) were prepared in a sequential manner as follows. Ligands **L1** and **L2** are commercially available, while **L3–L5** were synthesized according to procedures adapted from the literature (Scheme 1).[29] The pro-ligand HC^N was prepared through a two-step one-pot methodology (see Scheme S1†). First, a Pictet–Spengler protocol was applied by reacting tryptamine with benzaldehyde to obtain 1-phenyl-1,2,3,4-tetrahydro-β-carboline, which was then oxidized in the presence of Pd/C to obtain 1-phenyl-β-carboline.[30,31] On the other hand, the Ir(III) dimeric precursor of formula [Ir(μ-Cl)(C^N)$_2$]$_2$ was synthesized by reacting two equivalents of 1-phenyl-β-carboline (HC^N) with one equivalent of $IrCl_3{\cdot}3H_2O$ according to the classical procedure.[32,33]

The target cationic Ir(III) heteroleptic complexes of formula *rac*-[Ir(C^N)$_2$(N^N)]Cl (**IrL1–IrL5**) were obtained by refluxing the Ir(III) dimer [Ir(μ-Cl)(C^N)$_2$]$_2$ along with two equivalents of the respective N^N ligand, **L1–L5**, using a mixture of dichloromethane–methanol (2 : 1; v : v) as the solvent system (Scheme 1).[34] The products were isolated as chloride salts of the monocationic complexes containing equimolar mixtures of Δ and Λ enantiomers (racemate). All complexes were produced with good purities according to analytical and spectroscopic data and are air- and moisture-stable in the solid state. The solubility of **IrL1–IrL5** in polar organic solvents, such as MeOH, DMSO and DMF, is reasonably good, but very low in ACN.

2.2. Characterization of complexes

The composition and structure of **IrL1–IrL5** were established by multinuclear NMR, high-resolution mass spectrometry (HR-MS) and elemental analysis. The ^{1}H and ^{13}C{^{1}H} NMR spectra of **IrL1–IrL5** were recorded in DMSO-d$_6$. For each complex, the spectra displayed coordination-attributed shifts for some peaks compared to those of the free N^N ligands and a number of distinctive features (see the ESI†), such as: (a) one set of resonances for the two equivalent C^N ligands in agreement with the C_2-symmetry of these complexes; (b) one set of signals for the corresponding N^N ligand where every signal integrates as 2 H (C_2-symmetry); (c) one sharp singlet (2 H) around 12.1 ppm for the two equivalent N–H groups of both C^N ligands (δ 11.5 ppm for the free proligand, Fig. S1†).[35] High-resolution mass spectrometry (HR-MS) showed mass/charge ratios and isotopic distributions fully compatible with the molecular structures proposed in Scheme 1 for monocationic complexes (see spectra in the ESI†).

2.3. Crystal structure of [IrL2]Cl

The crystal structure of **[IrL2]Cl** was resolved by single-crystal X-ray diffraction. A single crystal suitable for crystallographic resolution was obtained by slow evaporation of a solution of **IrL2** in a ternary mixture of MeOH/CH_2Cl_2/acetonitrile. The complex crystallizes in the monoclinic *C*2/*c* space group. The unit cell contains four pairs of enantiomers (Δ,Λ) due to helical chirality. The ORTEP diagram for the molecular structure of **Λ-[IrL2]$^+$** is depicted in Fig. 1. Selected angles and bond distances together with standard deviations are compiled in Table S1† and important crystallographic parameters are gathered in Table S2.† The molecular structure of **Λ-[IrL2]$^+$** exhibits the expected pseudo-octahedral geometry with the classical *trans*-N,N and *cis*-C,C disposition for the two C^N ligands. Besides, it displays C_2-symmetry with one two-fold axis going through the Ir center and bisecting the N^N ligand.[36] The Ir–N bond distances for the N^N ligand (2.165(5) and 2.167(5) Å) are longer than those determined for the C^N ligands (2.053(5) and 2.096(6) Å), due to the strong *trans* influence attributed to metal-bonded phenyl rings.[37] Both Ir–C bond lengths are identical (2.015(6)) and within the expected range for this kind of complexes.[25,36] The bite angles of the chelate rings are also standard, that is 76.9(2)° for the phen ligand and 80.4(2)° and 80.9(2)° for the C^N ligands. The torsion angles of the N^N ligand (−2.18°) and the C^N ligands (9.94° and 6.03°) suggest a higher degree of coplanarity for phen, in comparison with the C^N metallacycles, which is attributed to the higher flexibility and relative steric hindrance in the latter.

The 3D lattice of the respective crystal structure is stabilized by multiple hydrogen bonding interactions (Table S3†), where the Cl$^-$ counterion acts as an acceptor and N–H and C–H groups play the role of donors. Double π,π-stacking contacts between benzene and pyrrole rings from adjacent β-carboline scaffolds have also been found (Fig. S23 and Table S4†).

2.4. Theoretical calculations

With the aim of understanding the photophysical properties of these compounds and rationalizing the observed trends within this family, the cation complexes **[IrL1]$^+$**–**[IrL5]$^+$** were studied using density functional theory (DFT). Calculations were executed at the B3LYP/(6-31GDP+LANL2DZ) level including solvent effects (water). The results obtained predicted a

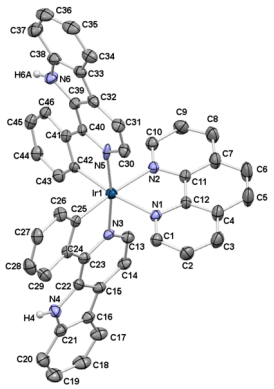

Fig. 1 ORTEP diagram for the molecular structure of **Λ-[IrL2]$^+$** obtained by single crystal X-ray diffraction. Thermal ellipsoids are shown at the 30% probability level. The respective Δ enantiomer, H atoms (except those of N–H groups) and the Cl$^-$ counterion have been omitted for the sake of clarity.

pseudo-octahedral geometry for **[IrL1]**$^+$–**[IrL5]**$^+$ in their respective ground electronic state (S_0) upon full optimization. The topology and energy of the MOs were also calculated for the ground electronic state (S_0) and are shown in Scheme 2 and Table S6.† In good agreement with the literature,[37–39] the HOMOs are composed of a mixture of orbitals from the iridium centre (d_π) and from the two phenyl rings of the C^N ligands (π orbitals). Moreover, all of them exhibit a π-antibonding nature at the Ir–C_{phenyl} interfaces. As long as the five Ir(III) complexes bear the same C^N ligand the energies calculated for the HOMO of all these derivatives are virtually identical (−5.32 to −5. 34 eV).

Also as expected, the LUMOs are distributed over the corresponding N^N ligand.[39] As shown in Scheme 2, the energy values calculated for the LUMO of **[IrL1]**$^+$ and **[IrL2]**$^+$ are nearly the same. However, the LUMO energies are stabilized on going from **[IrL2]**$^+$ (−2.04 eV) to **[IrL5]**$^+$ (−2.89 eV) as the number of π-conjugated rings in the N^N ligand is gradually extended from **[IrL2]**$^+$ to **[IrL5]**$^+$. Inexorably, this stabilization of the LUMO leads to a reduction in the HOMO–LUMO energy gap, from around 3.28 eV for **[IrL1]**$^+$ and **[IrL2]**$^+$ to 2.44 eV for **[IrL5]**$^+$. Moreover, the contribution of the two pyridyl rings in the respective LUMO is decreased progressively as π-conjugation is increased in the N^N ligands from **[IrL1]**$^+$ to **[IrL5]**$^+$.

The nature of the emitting excited state was investigated using the time-dependent DFT (TD-DFT) approach. The three lowest-energy triplet excited states (T_1, T_2 and T_3) were calculated (see Table S7†). For complexes **[IrL1]**$^+$–**[IrL3]**$^+$, the three lowest lying triplet excited states predicted for each complex are very similar in energy (**[IrL1]**$^+$: 2.51 eV, 2.54 eV, and 2.58 eV; **[IrL2]**$^+$: 2.52 eV, 2.54 eV, and 2.60 eV; **[IrL3]**$^+$: 2.50 eV, 2.53 eV, and 2.54 eV). On its part, **[IrL4]**$^+$ shows two triplet states close in energy (T_1 and T_2) but T_3 is at higher energies (2.27 eV, 2.29 eV and 2.51 eV). In contrast, triplet states calculated for **[IrL5]**$^+$ are well separated in terms of energy (1.43 eV, 2.05 eV, 2.42 eV), since T_1 and T_2 are significantly stabilized. Moreover, we investigated the nature of the absorption band with maxima around 410 nm using TD-DFT results (see Table S7†). For complexes **IrL1–IrL3**, this absorption band is attributed to ^{1}MLCT and ^{1}LC transitions between HOMO → LUMO+2 (S_2 for **IrL1** and S_3 for **IrL2**) and HOMO → LUMO+3 (S_4 for **IrL3**) with a calculated oscillator strength of 0.1495, 0.1554 and 0.1474, respectively. For **IrL4**, this absorption band is assigned to the singlet excite states S_6 and S_7. Both excited states correspond to HOMO → LUMO+1 (^{1}MLCT and ^{1}LLCT) and HOMO → LUMO+2 (^{1}MLCT and ^{1}LC) transitions, although S_7 has also a significant HOMO−4 → LUMO contribution. The calculated oscillator strengths for S_6 and S_7 were 0.0754 and 0.0795, respectively. **IrL5** displayed a singlet excited state S_8 that corresponds to HOMO → LUMO+3 transitions (^{1}MLCT and ^{1}LLCT) with a calculated oscillator strength of 0.1463. Compared to **IrL1–IrL4**, **IrL5** displayed a singlet excited state (S_2) that corresponds to HOMO−2 → LUMO transitions (^{1}LC) with a calculated oscillator strength of 0.0186, which is responsible for the long absorption tail observed for **IrL5** in the experimental absorption spectrum. In addition, **IrL5** displayed one strong absorption band around 330 nm that corresponds to ^{1}LC transitions between different MOs centred at the dppn ligand.

For a deeper comprehension of the nature of the lowest-energy triplet state, the geometry of this state was optimized

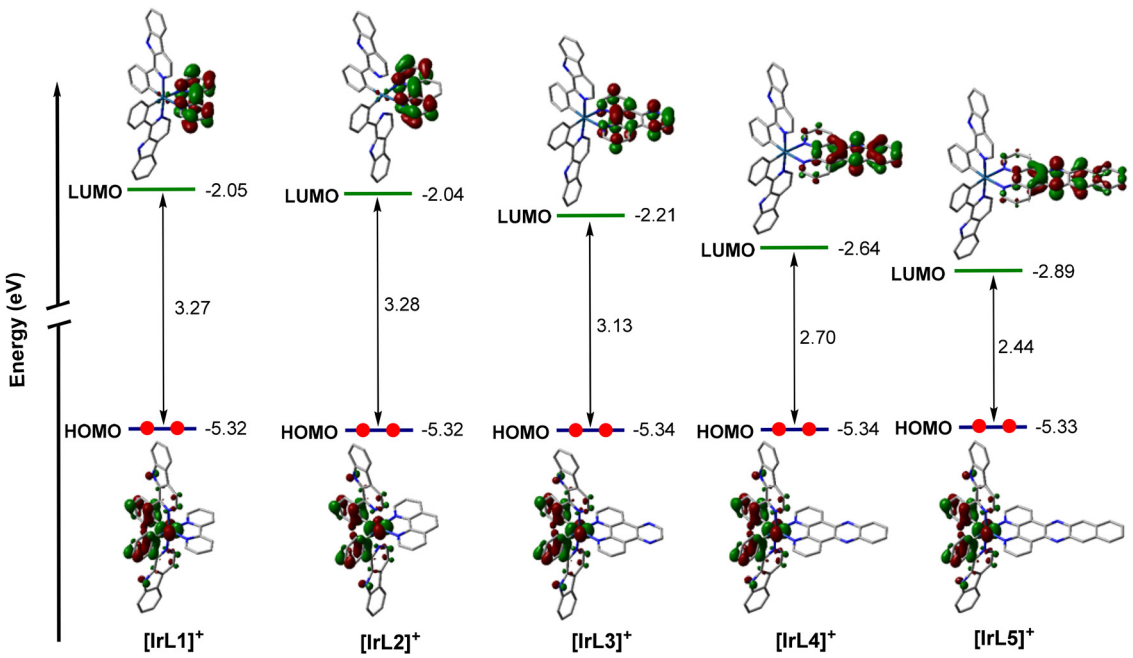

Scheme 2 Schematic representation showing the isovalue contour plots calculated for HOMOs and LUMOs of **[IrL1]**$^+$–**[IrL5]**$^+$.

using DFT calculations. Thus, the unpaired-electron spin-density was calculated for the fully relaxed triplet state in every case, showing that this state corresponds mainly to the HOMO → LUMO monoexcitations obtained in the TD-DFT calculations for **[IrL1]**$^+$–**[IrL4]**$^+$ (that is, **[IrL1]**$^+$: T_3; **[IrL2]**$^+$: T_3; **[IrL3]**$^+$: T_1; and **[IrL4]**$^+$: T_1). This indicates that the excitation implies the promotion of one electron from the Ir-phenyls environment to the ancillary N^N ligand (^{3}MLCT/^{3}LLCT) as illustrated in Fig. 2A. However, the unpaired-electron spin-density calculated for **[IrL5]**$^+$ is defined by the HOMO−2 → LUMO monoexcitation corresponding to the first triplet state predicted using TD-DFT calculations. Hence, the fully relaxed triplet state for **[IrL5]**$^+$ stems from the promotion of one electron located in a π orbital of dppn to a π-antibonding orbital of dppn, which involves a ^{3}LC transition (Fig. 2B).

The phosphorescence emission energies (E_{emS}) were estimated as the vertical energy difference between T_1 and S_0, both for the fully relaxed triplet state geometry. Notably, the trend observed in the calculated values for **IrL1–IrL4** is in good agreement with the tendency displayed by the experimental values obtained from the emission spectra (see Tables 1 and 2). Nonetheless, **IrL5** lacks emissive properties and therefore, its experimental E_{em} value has not been determined.

2.5. UV-vis absorbance spectra

The UV-vis absorption spectra of complexes **IrL1–IrL5** were recorded in aqueous solutions (H_2O : DMSO, 99 : 1, v : v, 10^{-5} M, pH = 6.8) at room temperature (Fig. 3). All the complexes display strong absorption bands with maxima around 250 nm that are attributed to spin-permitted ligand centred transitions (^{1}LC, π → π*, C^N and N^N ligands).[40] **IrL5** displayed one intense absorption band at around 330 nm that corresponds to ligand centred transitions in the dppn ligand (^{1}LC, π_{dppn} → π^*_{dppn}) (see Table S7†). Additional absorption bands were observed around 350 nm and are ascribed to ^{1}MLCT and ^{1}LLCT transitions. In the visible region, all complexes exhibit one absorption band with maxima or shoulders around 410 nm, showing a tail that spreads up to 525 nm (for **IrL1–IrL3**), 550 nm (for **IrL4**) and 600 nm (for **IrL5**). This settles that an increase in the number of aromatic rings in the respective N^N ligand causes the lengthening of this low energy absorption tail improving the capacity of the corresponding complexes to absorb light in the visible region. This band is attributed to a mixture of spin-allowed ^{1}MLCT, ^{1}LLCT and ^{1}LC transitions and spin-forbidden ^{3}MLCT and ^{3}LC transitions (see Table S7†).[25]

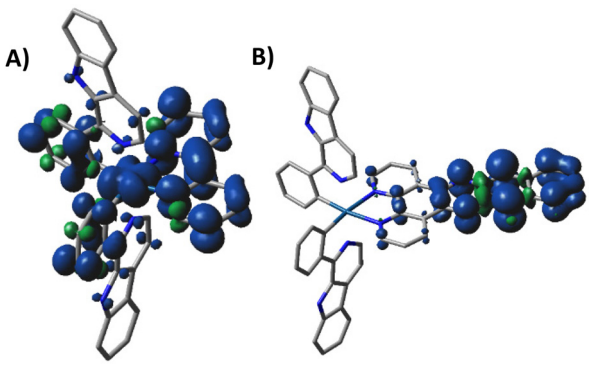

Fig. 2 Unpaired-electron spin-density contours (0.002 au) calculated for the fully relaxed triplet state of complexes **IrL1** (A) and **IrL5** (B).

Table 1 Adiabatic energy difference (Δ*E*) between S_0 and T_1 states for **IrL1–IrL5** and emission energy (E_{em}) estimated as the energy difference between T_1 and S_0 for the fully relaxed triplet state geometry of **IrL1–IrL5**

Compound	Δ*E* (eV; nm)	E_{em} (eV; nm)	HOMO–LUMO energy gap (eV)
IrL1	2.39; 519	2.13; 582	3.27
IrL2	2.35; 527	2.12; 584	3.28
IrL3	2.25; 551	2.01; 616	3.13
IrL4	1.98; 626	1.79; 693	2.70
IrL5	1.38; 898	1.10; 1127	2.44

Table 2 Photophysical properties of complexes in H_2O : DMSO (99 : 1, v : v) at room temperature under a nitrogen atmosphere

Complex	λ_{ex} (nm)	λ_{em} (nm)	τ [contribution] (ns)	Φ_{PL} (%)
IrL1	405	600	26 [21] 95 [79]	3.0
IrL2	405	601	23 [31] 81 [69]	3.4
IrL3	405	568	2 [19] 15 [81]	3.8
		609[a]	23 [100][a]	
IrL4	405	568 620[b]	2 [100]	0.69
IrL5	405	—	—	—

[a] Determined for a 5 × 10^{-6} M solution in H_2O : DMSO, 99 : 1, v : v, instead of 10^{-5} M solution. [b] Determined for a ×10^{-6} M solution in DMSO.

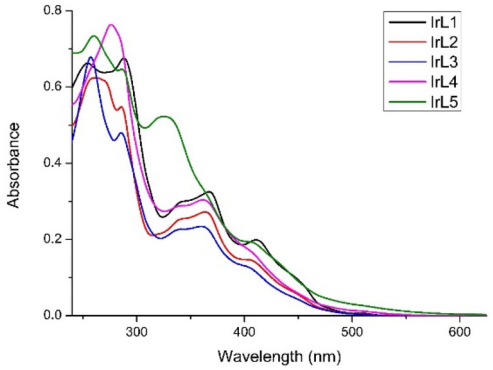

Fig. 3 Overlaid absorbance spectra of **IrL1–IrL5** (10^{-5} M) in H_2O : DMSO (99 : 1, v : v) at room temperature.

2.6. Emission and photophysical properties

The emission spectra of **IrL1–IrL4** were recorded for deoxygenated solutions (10^{-5} M) in H_2O : DMSO (99 : 1, v : v) at 25 °C

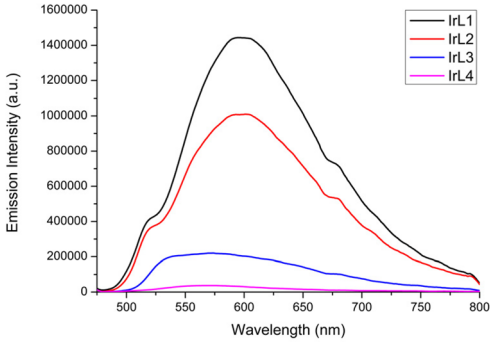

Fig. 4 Overlaid emission spectra of **IrL1–IrL4** in deoxygenated H_2O : DMSO (99 : 1, v : v) (10^{-5} M) at 25 °C under irradiation with λ = 405 nm.

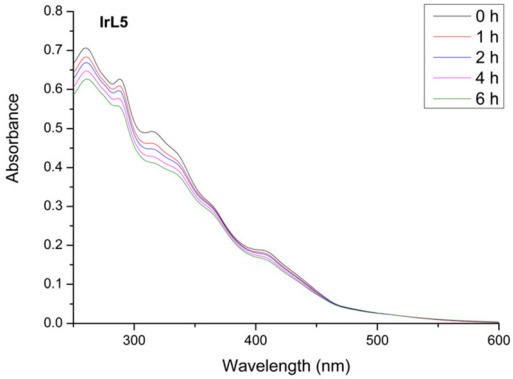

Fig. 5 Overlaid UV-vis absorbance spectra of **IrL5** (10^{-5} M) in H_2O : DMSO (99 : 1, v : v, pH = 6.8) at different times under blue light irradiation (0 h, 1 h, 2 h, 4 h, and 6 h) at room temperature.

under irradiation at λ_{ex} = 405 nm (Fig. 4 and Fig. S38†) for the normalized emission spectra). All the spectra showed broad emission bands with maxima centred between 568 nm and 620 nm (Table 2). The intensity of these bands is reduced gradually from **IrL1** to **IrL4**, as the π-conjugation of the respective N^N ligand is extended from **L1** (bpy) to **L4** (dppz). In contrast, complex **IrL5** did not show any emission process in aqueous solution under 405 nm excitation as previously seen for a similar derivative with dppn,[27] showing the non-emissive nature of its excited states. The effect of concentration on the emission spectra has been analysed for **IrL3** and **IrL4**. In particular, the spectrum of **IrL3** in H_2O : DMSO (99 : 1, v : v) at 5×10^{-6} M shows a broad band with λ_{em} = 609 nm with a shoulder at lower wavelengths. Moreover, the intensity of the emission band was drastically decreased at higher concentrations (Fig. S28†). **IrL4** exhibits a similar behaviour in DMSO (Fig. S29†). These findings revealed a self-quenching effect for the lower energy emission of **IrL3–IrL4**.[41–43]

The excited state lifetimes (τ) and photoluminescence quantum yields (Φ_{PL}) were experimentally determined only for complexes **IrL1–IrL4** (Table 2). The excited state lifetimes range from 2 ns for **IrL4** to 95 ns for **IrL1**. The photoluminescence quantum yields (Φ_{PL}) of these iridium complexes are very low with values of around 3% for **IrL1–IrL3** and 0.69% for complex **IrL4**, all of them near or below the limit of experimental error. The weak emission of similar complexes with **dppz** and **dppn** is a well-established feature.[27,44,45]

2.7. Photostability

The photostability of **IrL1–IrL5** was evaluated by monitoring the evolution with time of their UV-vis spectra recorded for 10^{-5} M solutions in H_2O : DMSO (99 : 1) under irradiation with blue light (LED, λ_{ex} = 460 nm, 24 W) and under air atmosphere at room temperature (Fig. 5 and Fig. S24†). A gradual decrease in the intensity of the spectra was observed, accompanied by the formation of one isosbestic point around 420–470 nm. Consequently, we concluded that after 6 hours under irradiation, these iridium complexes displayed moderate to high photostability with values of photodegradation between 11% and 20% (**IrL3**). We speculate that these observations could be consistent with the partial photodissociation of the C^N ligand due to the thermal population of ^{3}MC excited states, although other possibilities cannot be ruled out.[46]

2.8. Self-aggregation studies

It is well known that the presence of π-extended ligands in metal complexes promotes the formation of aggregates in solution through π,π-stacking interactions.[47,48] Ligands such as **L3–L5** are prone to establish this type of interaction which can modify both the photophysical properties and the cellular uptake of their respective complexes.

First, the self-aggregation trends of **IrL4** and **IrL5** were studied by ^{1}H-NMR spectroscopy. The ^{1}H NMR spectra of **IrL4** and **IrL5** were recorded in DMSO-d_6 at two different concentrations (2.5 mM and 25 mM). As shown in Fig. 6 and Fig. S30† for **IrL5** and **IrL4**, respectively, the chemical shifts attributed to the protons of the respective N^N ligand (**L5** and **L4**) are dependent on the concentration. More specifically, these peaks are shifted upfield in the high concentration spectra (25 mM) compared to those recorded in the diluted spectra (2.5 mM). This effect is ascribed to the shielding caused by π,π-stacking interactions between the N^N ligands of different Ir molecules.[22,49–51] In contrast, the resonances of the aromatic protons of the C^N ligands are either, not shifted, or only slightly shifted downfield. Therefore, these results confirm the tendency of **IrL4** and **IrL5** to form self-aggregates mediated by π,π-stacking interactions when the concentration is increased. This observation was corroborated through DOSY experiments which provided different diffusion coefficients for the two studied concentrations (2.5 mM and 25 mM) in the case of **IrL5** (Fig. S31†).

Then, with the aim of analysing the impact of self-aggregation in the photophysical and biological properties of these PSs, we search for possible deviations from the Lambert–Beer law through UV-vis spectroscopy for a H_2O : DMSO (99 : 1) solution of **IrL5** in the concentration range between 1 and 30 μM. Thus, when plotting absorbance at two different wavelengths

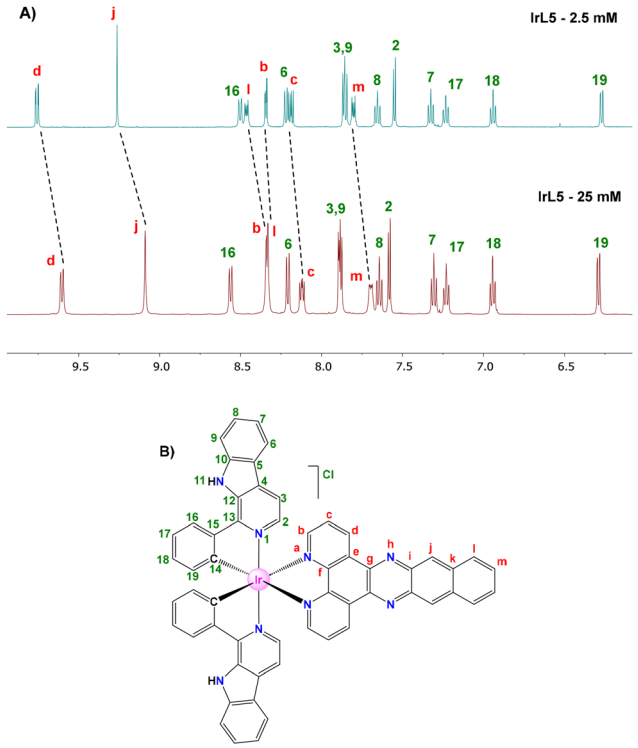

Fig. 6 (A) ^{1}H NMR spectra of **IrL5** in DMSO-d_6 at 25 °C at either 2.5 mM (above) or 25 mM (below). (B) Atom labelling used in proton assignment.

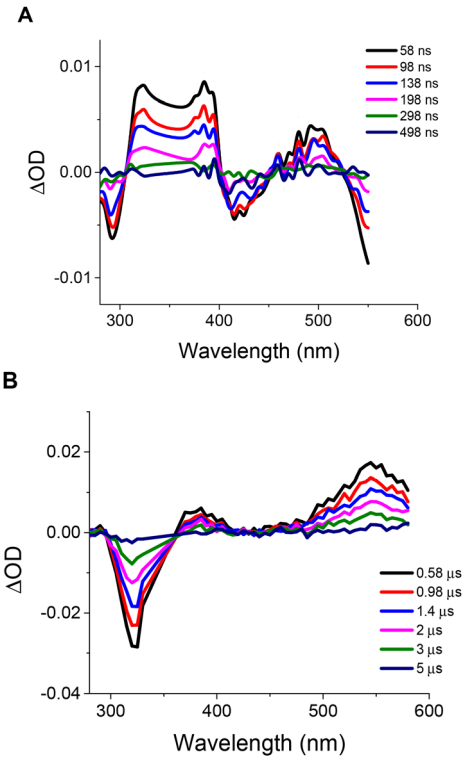

Fig. 7 Transient absorption spectra of **IrL1** (A) and **IrL5** (B) in DMSO : H_2O (1 : 1, v : v). Ground state absorption was matched at the laser excitation wavelength for both compounds (Fig. S33†).

(323 and 405 nm) *versus* concentration we obtained good linear fits in both cases (Fig. S32†). This result demonstrates that for the concentration range used in the determination of the photophysical properties and the biological studies self-aggregation is negligible.

2.9. Transient absorption spectroscopy

We implemented nanosecond transient absorption spectroscopy (TAS) measurements aiming to determine the excited state lifetime of the non-emissive complex **IrL5** and also to reveal its quenching behaviour in the presence of O_2. For comparison purposes we included complex **IrL1** in the study as a representative of the emissive complexes (**IrL1–IrL4**), with the purpose of exploring further the divergent biological behaviour of **IrL5** compared to **IrL1–IrL4** (*vide infra*). The TAS spectra of both complexes were recorded in DMSO : H_2O (1 : 1, v : v) upon laser excitation at 355 nm. The TAS spectrum of **IrL5** featured three different regions (Fig. 7B): one bleaching range due to the ground state depletion, where the optical density change is negative (300–370 nm), and two excited state absorptions, *i.e.*: 370–410 nm and 410–600 nm, respectively. **IrL1** displays a different TAS profile with the following ranges (Fig. 7A): (a) two regions of negative optical density registered at 290 and 410 nm that correspond to ground state depletions; (b) one region between 310 and 400 nm, where **IrL1** presents strong excited state absorption, overlapping the ground state absorption bands; (c) an excited state absorption band between 440 and 520 nm (ground state absorption is minimal at these wavelengths); (d) at wavelengths higher than 515 nm, the negative transients are due to the emission from **IrL1**.

Then, we conducted kinetic studies for both the recovery of the negative transients at 290 and 320 nm and the decay of the positive transients at 490 and 540 nm for **IrL1** and **IrL5**, respectively (Fig. S34†). Thus, we concluded that the acquired transients (excited states) at negative and positive optical density values yielded the same lifetimes which confirms that both features correspond to the relaxation of the same excited state. To determine the possible influence of O_2 on the lifetime of the respective transients, we carried out similar kinetic experiments upon bubbling argon. Thus, we observed that the lifetime for **IrL1** is only slightly affected by the presence of O_2 (102 ns *vs.* 118 ns in the absence of O_2, Table S8†) and compares well with that obtained from emission experiments (95 ns), evidencing that all the experimental observations are attributable to the same excited state. However, for **IrL5** the situation is entirely different, since the lifetime is substantially increased in the absence of O_2 (1770 ns *vs.* 4130 ns, respectively, Table S8†). Furthermore, the observed negative (bleaching) and positive (transient absorption) optical density variations, decay to zero, indicating that no other species is being formed throughout the experiments. As a consequence the observed quenching by oxygen (decrease in the lifetime in the presence of O_2), is consistent with an energy transfer process to oxygen.

All in all, for **IrL1**, the experimental results are consistent with the formation of an emissive short-lived transient, which

we cannot exclude to be a triplet, T_1, presenting very small quenching by O_2. In contrast, **IrL5** exhibits a non-emissive long-lived transient, with a clear triplet behaviour, which is strongly quenched by O_2 through an energy transfer process, meaning that singlet oxygen ($^1O_2$) is the main species formed in the process.[52] Scheme 3 shows a complete picture of excited states for **IrL1** and **IrL5**.

2.10. Singlet oxygen generation

The capacity of **IrL1–IrL5** to generate singlet oxygen ($^1O_2$) was experimentally determined in H_2O : DMSO (1 : 1) using 9,10-anthracenediyl-bis(methylene)dimalonic acid (ABDA, 8×10^{-5} M) as a very specific probe. This compound reacts *in situ* with one molecule of singlet oxygen generated photocatalytically from the interaction of $^3O_2$ with the photosensitizer (10^{-5} M) to form an endoperoxide (Scheme S2†).[53,54] The reaction was monitored by UV-vis and the gradual decrease of the maximum at 379 nm was used to quantify the ability of our complexes to generate singlet oxygen (Fig. 8, 9 and Fig. S35†). Thus, the singlet oxygen quantum yields (Φ_Δ) of **IrL1–IrL5** under blue light irradiation (λ_{ir} = 460 nm) were determined using Rose Bengal (Φ_Δ = 0.75) as the reference[55] and are gathered in Table 3 and Table S9.† Consistent with the TAS studies and the ^{3}LC nature of its excited state, **IrL5** features an outstanding Φ_Δ around 1, whereas **IrL1–IrL4** show moderate performance in this regard, with Φ_Δ values between 0.10 and 0.29, suggesting a rough correlation between $^1O_2$ production and excited-state lifetimes as reported for other Ir PSs.[18] Moreover, a control experiment was performed in the absence of a photosensitizer to corroborate the remarkable photostability of ABDA upon blue light irradiation (see Fig. S35†).

2.11. Photocatalytic oxidation of NADH

NADH is a cofactor that plays a major role as an electron donor in the mitochondrial electron transport chain (ECT) and

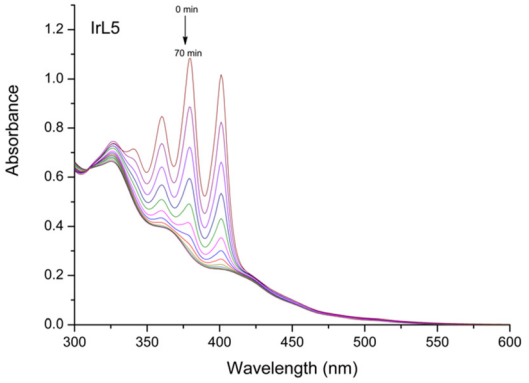

Fig. 8 Photobleaching of ABDA (8×10^{-5} M) in the presence of **IrL5** (10^{-5} M) in H_2O : DMSO (1 : 1) under blue light irradiation (460 nm, 24 W) for 70 min at room temperature.

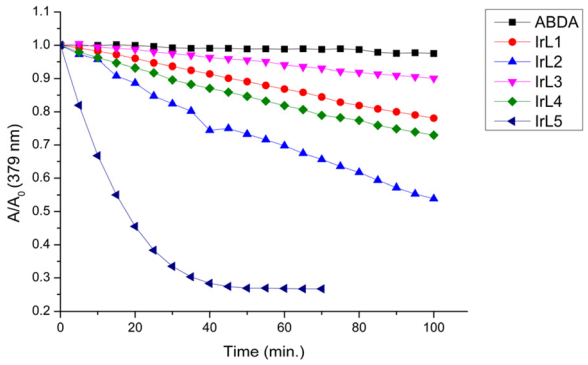

Fig. 9 Comparison of the photobleaching rates of ABDA (8×10^{-5} M) in the absence and presence of **IrL1–IrL5** (10^{-5} M) in H_2O : DMSO (1 : 1) under blue light irradiation.

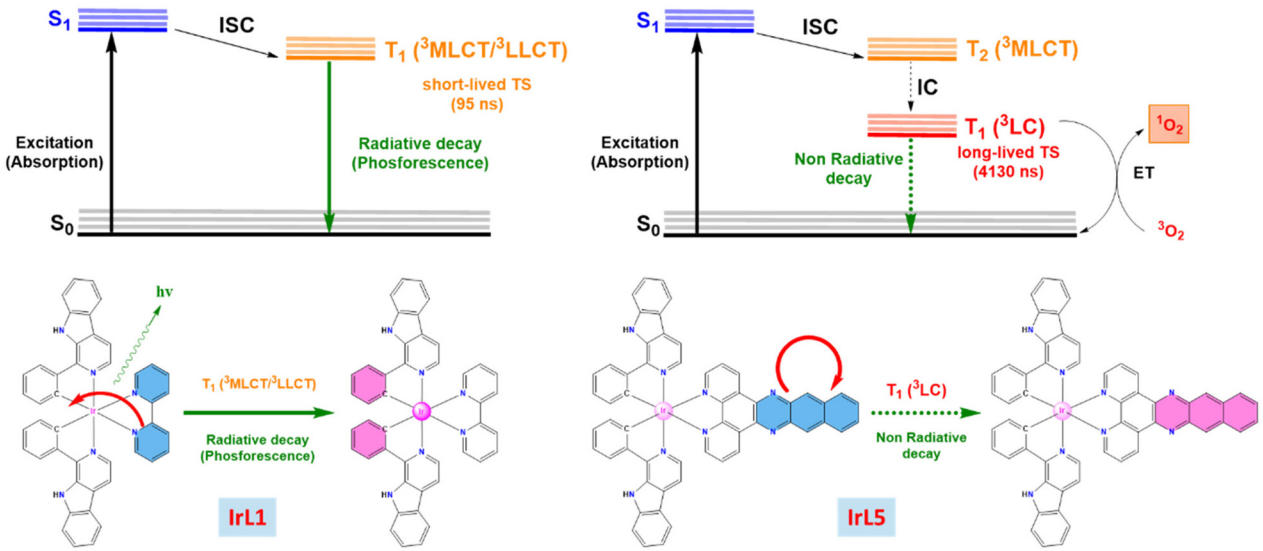

Scheme 3 Illustration of the lowest-lying triplet excited states of complexes **IrL1** and **IrL5**.

Table 3 Singlet oxygen quantum yields of complexes **IrL1–IrL5** (10^{-5} M) using **RB** as a reference

Complex	Φ_Δ	Excited state lifetime (ns)
RB	0.75	
IrL1	0.11	95
IrL2	0.29	81
IrL3	0.10	23
IrL4	0.17	2
IrL5	1.02	4130

its photocatalytic depletion can be directly related to the depolarization of mitochondria as has been shown recently by different groups.[56,57] Consequently, this type of photoactivated oxidative stress can trigger mitochondrial oxidation-induced cell death in cancer cells. In an effort to determine a potential molecular target for our complexes, we monitored the photocatalytic oxidation of an aerated solution of NADH (0.1 mM) in H_2O : DMSO (99 : 1) in the presence of **IrL5** (5 μM) by UV-vis spectroscopy under blue light irradiation (λ_{ir} = 460 nm) for a period of 15 min. Thus, under photoirradiation we observed a gradual and fast decrease of the absorbance band at 338 nm (Fig. 10), attributed to NADH, which is consistent with the formation of the respective oxidized form of this cofactor, NAD^+. Two control experiments in the absence of either **IrL5** (Fig. S36†) or light irradiation (Fig. S37†) allowed us to reveal the photocatalytic nature of this oxidation process.

2.12. Cell internalization

The biological characterization of the complexes began by determining their internalization kinetics into cells, which is a crucial process for the subsequent antitumor activity. This study was carried out with complexes **IrL1–IrL3** since the phosphorescence of **IrL4** and **IrL5** was markedly attenuated under the cell culture conditions. A549 cells were incubated with the complexes at a concentration of 5 μM for different periods ranging from 10 minutes to 6 hours, and the fluorescence emission from the cells, which corresponds to the internalization of the complexes, was determined by flow cytometry. After only 10 minutes of treatment, cellular fluorescence was already detected, revealing very rapid internalization of the complexes. Over the next 4 hours, cellular fluorescence progressively increased, indicating a continuous uptake rate. However, after 4 hours, a minimal increase in the fluorescence intensity was observed for the three complexes (Fig. 11A and B). Based on these results, it was established an incubation period of 4 hours before irradiation for subsequent studies in order to achieve optimal cellular accumulation of the complexes and, consequently, enhance their phototoxic efficiency.

To compare the cellular internalization of the different complexes, A549 cells were exposed to **IrL1–IrL5** at an equimolar concentration of 5 μM for 4 h and the amount of iridium inside the cells (ng Ir per 10^6 cells) was quantified by ICP-MS. As shown in Fig. 11C, the presence of one or two aromatic rings fused to the bipyridine scaffold in complexes **IrL2** and **IrL3**, respectively, significantly increased their internalization efficiency by more than three times compared to **IrL1**, with values of 98.9 ± 2.4 ng Ir per 10^6 cells and 100.9 ± 25.8 ng Ir per 10^6 cells, respectively, relative to 33.1 ± 12.3 ng Ir per 10^6 cells for **IrL1**. This suggests that the lipophilicity of the complexes plays a role in their cellular accumulation to some degree. However, the amount of iridium inside the cells was lower in the case of **IrL4** and **IrL5** (6.7 ± 2.2 ng Ir per 10^6 cells and 7.1 ± 1.4 ng Ir per 10^6 cells, respectively).[58]

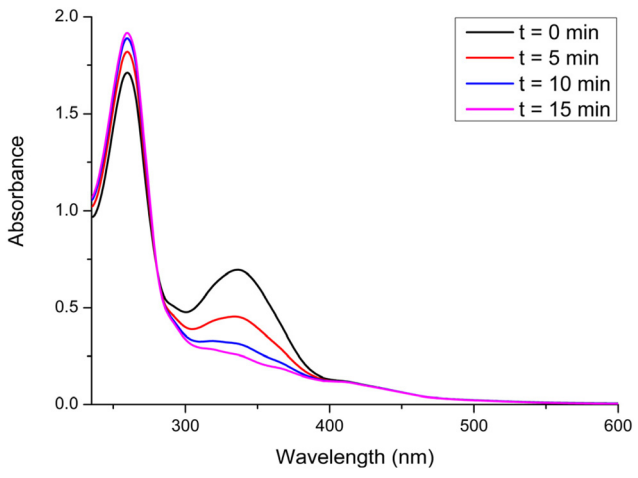

Fig. 10 UV-vis spectra for the photocatalytic oxidation of NADH (100 μM) in the presence of **IrL5** (5 μM) in H_2O : DMSO (99 : 1) under an air atmosphere and blue light irradiation (460 nm, 24 W) at room temperature.

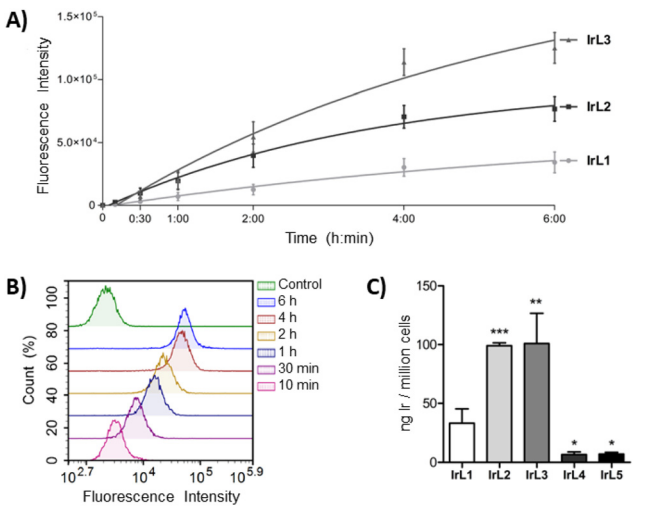

Fig. 11 Cellular internalization of complexes. A549 cells were incubated with complexes **IrL1–IrL3** at 5 μM. (A) The internalization kinetics were determined by measuring the median fluorescence intensity (at a λ value of 675 nm) of 10 000 cells at the indicated time intervals using flow cytometry. (B) Representative flow cytometry histograms of **IrL1** internalization at each time interval. (C) The amount of iridium per million cells after 4 hours of treatment was determined by ICP-MS. Each bar in the graph represents the mean ± SD of three independent experiments *p < 0.05; **p < 0.01; and ***p < 0.001 *vs.* **IrL1**.

2.13. Photocytotoxicity

The antiproliferative activity of **IrL1–IrL5** was evaluated in A549, HeLa and PC3 cancer cells as well as MRC-5 fibroblasts both under dark conditions and after blue light irradiation. In the dark, complexes **IrL1–IrL4** showed superior antitumor activity than the chemotherapeutic drug cisplatin in both A549 and PC-3 cell lines, with $IC_{50,dark}$ values ranging from 0.28 to 3.9 μM (Table 4). In HeLa cells and MRC-5 fibroblasts, slightly higher $IC_{50,dark}$ values of 0.81 to 9.4 μM and 0.65 to 7.6 μM, respectively, were obtained. It should be noted that **IrL3** exhibited the lowest $IC_{50,dark}$ values in all cell lines, which were in the nanomolar range. This is in accordance with the high intracellular internalization level of this complex. Conversely, **IrL5** demonstrated the lowest dark cytotoxicity, which is also consistent with its low level of cellular uptake.

The cytotoxic activity of all the complexes was enhanced by blue light irradiation, resulting in nanomolar $IC_{50,light}$ values for complexes **IrL1–IrL3** in all cell lines, and for **IrL5** in A549 and PC-3 cells (Table 4). Based on these values, the phototoxic indexes (PIs) were determined to identify the most effective complex for PDT. The highest PI values, ranging from 15 to 38, were obtained for **IrL5**. This result was positively correlated with the long excited state lifetime and remarkable ability to generate $^1O_2$ (*vide supra*) of **IrL5** and resembles the behaviour of related Ru (II) complexes with dppn.[2] Thus, the low cellular uptake of this complex is widely offset by its high Φ_Δ, compared to the rest of the iridium complexes in the family. **IrL2**, which exhibited the second higher capacity to generate singlet oxygen and a good cellular uptake, also increased considerably its cytotoxicity after irradiation resulting in PI from 6.8 to 19.7. **IrL1** and **IrL3** showed lower PIs, ranging from 3.04 to 9.8 and from 1.8 to 7.6, respectively. In contrast, **IrL4** which displayed a lower capacity to generate singlet oxygen, barely increased its cytotoxicity under blue light irradiation (PI ranging from 0.82 to 1.9). The results also indicated that, in general, these iridium complexes do not exhibit selective photodynamic activity against tumour cells compared to non-malignant fibroblasts.

In addition, the toxicity of complexes **IrL1–IrL5** against red blood cells (RBCs) was evaluated by haemolysis experiments. To this end, porcine RBCs were incubated with the complexes at their $IC_{50,light}$ values, both in the dark and under blue light irradiation. The results revealed that the haemolytic activity of the complexes was less than 1% under either of these conditions. This finding underscores the blood compatibility of our PSs at their $IC_{50,light}$ values, which is a crucial determinant of their practical utility in biomedical applications.

2.14. Colony formation

To further assess the antitumor effect of the complexes, clonogenic assays were carried out. These assays evaluate the ability of single cells to survive upon treatment and reproduce to form colonies. HeLa cells were selected for these experiments as they showed the best ability to grow as colonies. The cells were incubated with complexes **IrL1–IrL5** at the corresponding $IC_{50,light}$ for 4 hours and then irradiated with blue light or kept in the dark for 1 hour. The cells were immediately harvested, seeded at a low density, and allowed to grow to form colonies. Following treatments in the absence of irradiation, the number of colonies was similar to that of control untreated cells, except for complex **IrL4**, which significantly decreased the number of colonies to 51.5 ± 2% (Fig. 12). This result was expected, since the $IC_{50,light}$ and $IC_{50,dark}$ values of **IrL4** were very close. Upon light irradiation, the number of colonies decreased to 51.5 ± 4% for **IrL1**, 39.1 ± 2% for **IrL2**, 39.6 ± 4% for **IrL3**, 46.7 ± 3% for **IrL4** and 45.7 ± 2% for **IrL5** compared to control cells. These results validated the anticancer efficacy of these complexes. Furthermore, they disclosed that cellular damage is produced during photoactivation, given that the complexes were promptly removed following irradiation.

2.15. Intracellular localization by confocal microscopy

The distribution of the complexes inside the cells was studied by confocal microscopy. **IrL1** was selected for these experiments since it exhibited the highest emission intensity (Fig. 4). A549 cells were incubated with **IrL1** in the presence of the commercial dyes MitoView™ Green and LysoTracker™ Green DND-26 for mitochondria and lysosome localization, respectively. After one hour of incubation, confocal microscopy images of the cells showed a dotted red fluorescence corresponding to **IrL1** throughout the cytosol of the cells (Fig. 13). The overlap between the red fluorescence and the green fluorescence of MitoView™ Green, shown in yellow in the merged image, revealed that **IrL1** princi-

Table 4 Phototoxic activity of complexes **IrL1–IrL5** expressed as IC_{50} (μM)

Cell line	A549			HeLa			PC3			MRC-5		
	$IC_{50,dark}$	$IC_{50,light}$	PI	$IC_{50,dark}$	$IC_{50,light}$	PI	$IC_{50,dark}$	$IC_{50,light}$	PI	$IC_{50,dark}$	$IC_{50,light}$	PI
IrL1	1.9 ± 0.2	0.31 ± 0.1	6.0	9.4 ± 1	0.96 ± 0.09	9.8	3.9 ± 0.2	1.3 ± 0.04	3.0	7.6 ± 0.2	0.92 ± 0.1	8.3
IrL2	0.48 ± 0.07	0.046 ± 0.01	10.3	5.6 ± 0.9	0.33 ± 0.09	17	1.7 ± 0.3	0.25 ± 0.03	6.8	7.6 ± 0.9	0.39 ± 0.04	19.7
IrL3	0.28 ± 0.01	0.037 ± 0.01	7.6	0.81 ± 0.1	0.16 ± 0.04	5.0	0.51 ± 0.1	0.16 ± 0.04	3.1	0.65 ± 0.1	0.37 ± 0.08	1.8
IrL4	2.5 ± 0.3	1.3 ± 0.1	1.9	3.6 ± 0.7	2.4 ± 0.05	1.5	2.9 ± 0.1	2.2 ± 0.08	1.3	1.9 ± 0.2	2.4 ± 0.2	0.8
IrL5	18 ± 2	0.97 ± 0.04	19	15 ± 3	1.01 ± 0.05	15	28 ± 2	0.74 ± 0.06	38	22 ± 1	1.0 ± 0.1	22
Cisplatin	5.9 ± 1.2	—	—	1.5 ± 0.3	—	—	5.6 ± 1	—	—	5.3 ± 0.4	—	—

Cells were incubated with the compounds for 4 h at 37 °C and then kept in the dark or exposed to blue light (460 nm) for 1 h (24.1 J cm^{-2}). Cell viability was assessed after 48 h of treatment by MTT assays. Data represent the mean ± SD of at least three independent experiments, each performed in triplicate. PI = $IC_{50,dark}/IC_{50,light}$.

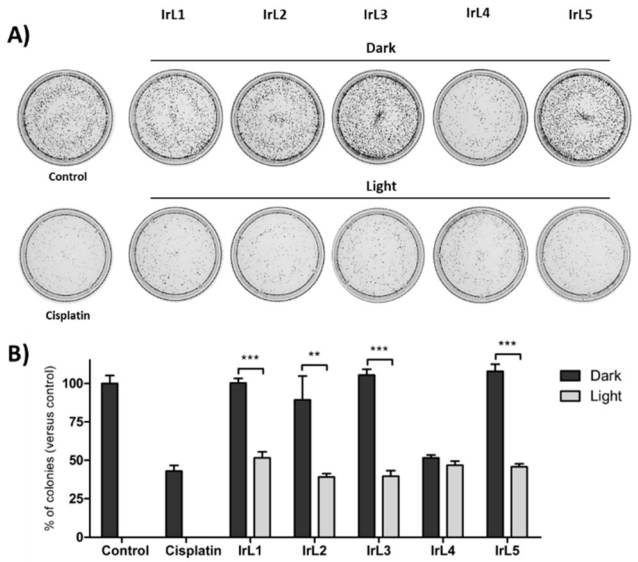

Fig. 12 Clonogenic assay. (A) Colony formation after exposure of HeLa cells to complexes **IrL1–IrL5** at the corresponding $IC_{50,light}$ under light and dark conditions. Control cells were treated with the medium alone. Cisplatin at 10 μM was used as the positive control. (B) Bar charts represent the percentage of colonies after each treatment relative to control cells (mean ± SD of 3 experiments, $^{**}p < 0.01$ and $^{***}p < 0.001$ *vs.* control cells).

pally accumulates in mitochondria, with a high Pearson co-localization coefficient (PCC) of 0.75. In contrast, the low degree of overlap between the green vesicular fluorescence of LysoTracker™ Green and **IrL-1**, with a PCC of 0.35, indicates that the distribution of the complex into lysosomes is minimal.

The mitochondrial targeting ability of **IrL1**, and presumably its congeners, is probably due to the combination of cationic and lipophilic features in its molecular structure. These features are a cationic iridium core together with an environment of aromatic organic ligands, respectively. Indeed, it is well-established that lipophilic cations show high affinity for mitochondria and tend to accumulate in the mitochondrial matrix. The driving force for this inward mitochondrial transport is provided by the high mitochondrial transmembrane potential (MMP) in functional mitochondria, which is generated by proton pumping into the intermembrane space during the ECT.[59,60] Indeed, many Ir(III) biscyclometalated complexes exhibit similar intracellular localization patterns.[26,61–64]

2.16. Effects on mitochondria

The MMP is essential for a suitable mitochondrial function, and consequently, for the generation of energy in the form of ATP, the transport of molecules across the mitochondrial membrane, the redox reaction balance, and the regulation of

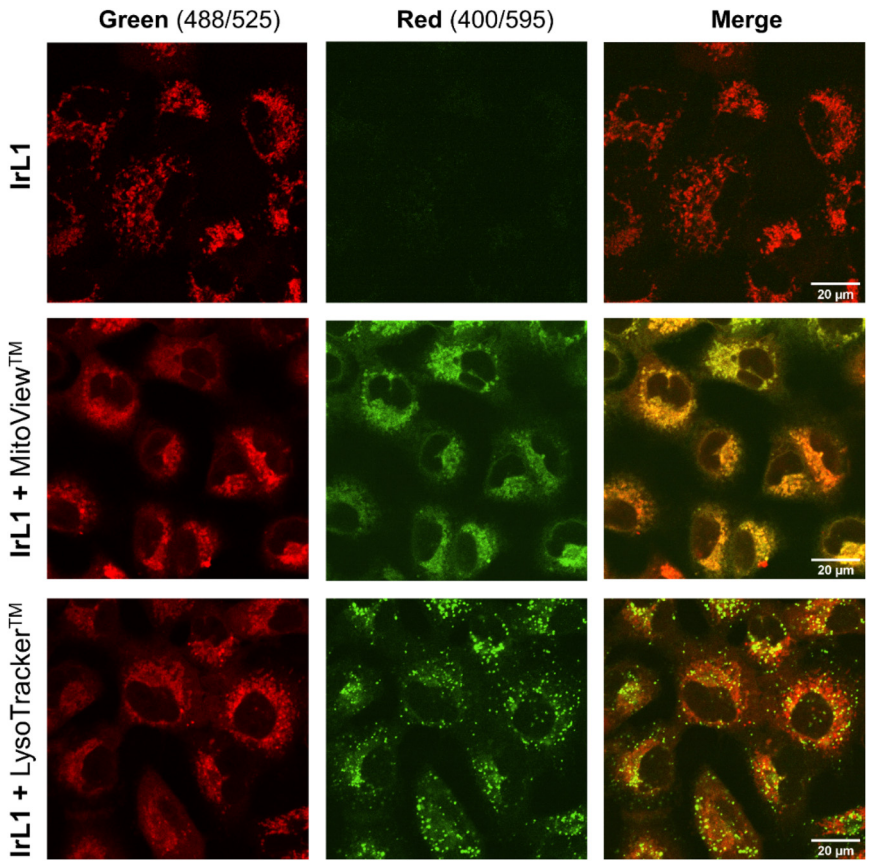

Fig. 13 Confocal microscopy imaging of the subcellular distribution of **IrL1**. A549 cells were incubated with **IrL1** (λ_{ex}: 400 nm; λ_{em}: 595 nm) at 25 μM for 1 h at 37 °C. The commercial dyes MitoView™ Green (λ_{ex}: 490 nm; λ_{em}: 523 nm) and LysoTracker™ Green DND-26 (λ_{ex}: 504 nm; λ_{em}: 511 nm) were used to localize the cellular distribution. Merged images show the fluorescence overlap in yellow. Scale bar: 20 μm.

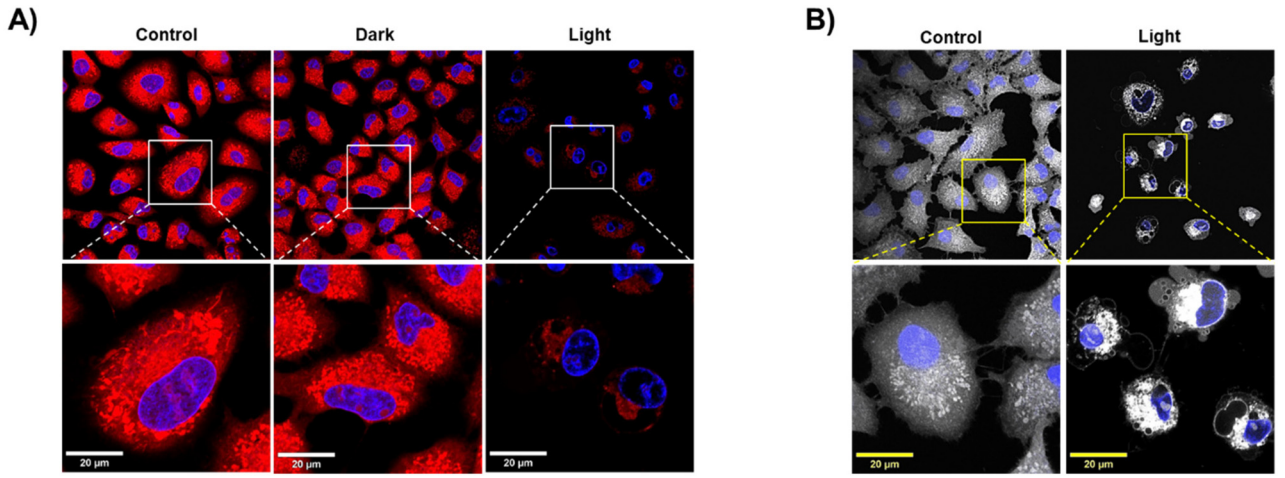

Fig. 14 Effect on mitochondria. A549 cells were incubated with **IrL5** at $IC_{50,light}$ (1 μM) for 4 h at 37 °C and then kept in the dark or exposed to blue light for 1 h. (A) The cell nuclei were localized in blue with Hoescht (λ_{ex}: 350 nm; λ_{em}: 461 nm), and healthy mitochondria were labelled with MitoTracker™ Red CMXRos (λ_{ex}: 579 nm; λ_{em}: 599 nm). Microscopy images show that photoactivation of **IrL5** severely affects the red fluorescence emission, indicating mitochondrial membrane depolarization. (B) Light irradiation caused membrane blebbing, which is a typical feature of apoptosis. The insets show a 3× magnification of the cells. Scale bar: 20 μm.

different signalling pathways including apoptosis.[59] Hence, depolarization of the mitochondrial membrane is a major indicator of mitochondrial damage and can significantly impact cell viability. Previous experiments (Fig. 10) demonstrated that coenzyme NADH can be photo-catalytically oxidized by **IrL5**, which can severely impair the mitochondrial ECT and dissipate the MMP. To explore the effect of **IrL5** at the mitochondrial level, A549 cells were incubated with **IrL5** at $IC_{50,light}$ (1 μM) for 4 h at 37 °C and then kept in the dark or irradiated with blue light for 1 h. Mitochondria were labelled with the red-fluorescent dye MitoTracker™ Red CMXRos. Importantly, the accumulation of this dye depends on the MMP of healthy mitochondria.[65] Cell nuclei were localized with Hoescht. The microscopy images presented in Fig. 14 showed intense red fluorescence emission from healthy mitochondria in both untreated control cells and cells treated with **IrL1** under dark conditions. However, upon light irradiation, there was a significant reduction of the red fluorescence, indicating depolarization of the mitochondrial membrane. This suggests that the photocatalytic oxidative activity of the complexes, together with their high affinity for mitochondria, leads to severe mitochondrial toxicity, which may be the primary mechanism of cell death. In fact, microscopy images also revealed that in response to photoactivated complexes, membrane blebbing was rapidly generated. This characteristic feature of apoptosis indicates that the photodynamic activity of the complex can rapidly trigger programmed cell death.[66]

3. Experimental

3.1 General information

All synthetic manipulations for Ir(III) complexes were carried out under an atmosphere of dry, oxygen-free nitrogen using standard Schlenk techniques. The solvents were dried and distilled under a nitrogen atmosphere before use. Elemental analyses were performed with a Thermo Fisher Scientific EA Flash 2000 elemental microanalyzer. UV-vis absorption was measured using a Jasco V-750 UV-visible spectrophotometer. Fluorescence steady state and lifetime measurements were performed in an FLS980 (Edinburgh Instruments) fluorimeter with a 450 W Xenon Arc Lamp and TCSPC laser, respectively. The quantum yield was determined using an FLS980 (Edinburgh Instruments) with a 450 W Xenon Arc Lamp and a red PMT sphere as the detector. HR-ESI(+) mass spectra were recorded with an Agilent LC-MS system (1260 Infinity LC/6545 Q-TOF MS spectrometer) using DCM as the sample solvent and H_2O (0.1% formic acid)/MeOH (0.1% formic acid) in a ratio of 30 : 70 as the mobile phase. The experimental *m*/*z* values are expressed in Da compared with the *m*/*z* values for monoisotopic fragments. NMR spectra were recorded at 298 K using a Bruker Avance III (300.130 MHz for ^{1}H; 75.468 MHz for ^{13}C) or Bruker Avance Neo 4500 (500.130 MHz for ^{1}H; 125.758 MHz for ^{13}C). ^{1}H NMR spectra were recorded with 32 scans into 32 k data points over a spectral width of 16 ppm. ^{1}H and ^{13}C{^{1}H} chemical shifts were internally referenced to TMS *via* the residual ^{1}H and ^{13}C signals of DMSO-d_6 (δ = 2.50 ppm and δ = 39.52 ppm), according to the values reported by Fulmer *et al.*[67] Chemical shift values (δ) are reported in ppm and coupling constants (J) in Hertz. The splitting of proton resonances in the reported ^{1}H NMR data is defined as s = singlet, d = doublet, t = triplet, q = quartet, m = multiplet, and bs = broad singlet. 2D NMR spectra were recorded using standard pulse sequences. All NMR data processing was carried out using MestReNova version 10.0.2.

3.1.1 Starting materials. The synthesis of Ir(III) precursor and ligands is well described in the ESI.† $IrCl_3 \cdot xH_2O$ was purchased from Johnson Matthey and used as received. The

reagents tryptamine, 2,2′-bipyridyl, palladium (10%) on carbon powder, and benzaldehyde were purchased from Sigma-Aldrich; 1,10-phenantroline monohydrate, ethylenediamine, 1,2-phenylenediamine, and 2,3-diaminonaphthalene were purchased from TCI Chemicals. All of them were used without further purification. Deuterated solvents (DMSO-d_6) were obtained from Eurisotop. Conventional solvents such as diethyl ether (Fisher Scientific), 2-ethoxyethanol (Acros Organics), ethanol (Scharlau), methanol (Scharlau), dichloromethane (Scharlau), and anisole (Acros Organics) were degassed and in some cases distilled prior to use.

3.2 Cell culture

The A549 lung carcinoma, HeLa cervical carcinoma, and PC-3 prostate adenocarcinoma cell lines were used to assess the antitumor activity of the complexes. MRC-5 lung fibroblasts were used as a non-cancer cell model. All cell lines were obtained from the American Type Culture Collection (ATCC). Cells were cultured in Dulbecco's modified Eagle's medium (DMEM) (Corning) supplemented with 10% foetal bovine serum (FBS) (Gibco-BRL) and 1% L-glutamine–penicillin–streptomycin (Cultek) at 37 °C in a Heracell 150 incubator (Thermo Fisher Scientific) with a humidified atmosphere containing 5% CO_2. Mycoplasma contamination was regularly controlled with a Mycoplasma Gel Detection Kit (Biotools). Commercial pig blood was obtained from Norfrisa.

3.3 Cellular internalization

Cellular uptake of the complexes was evaluated using A549 cells. The cells were seeded in 6-well plates (Sarstedt) at a density of 2 million cells per well and allowed to attach overnight. The cells were treated for 4 hours with **IrL1–IrL5** complexes diluted in culture medium at 5 μM or with medium alone as a control. After treatment, the cells were washed with a phosphate buffered saline (PBS) solution and harvested by trypsinization. The samples were centrifuged and washed three more times with PBS. The amount of iridium in each sample was determined by inductively coupled plasma mass spectrometry (ICP-MS) analysis. Previously, cell pellets were dissolved in 400 μL of 69% v : v nitric acid (PanReac Applichem) and heated at 100 °C for 18 hours. After cooling, the samples were diluted with Milli-Q water to a final volume of 10 mL. The iridium content was measured using an ICP-MS Agilent 7500c instrument at the Serveis Tècnics de Recerca, Universitat de Girona. The iridium standards were freshly prepared in Milli-Q water with 2% HNO_3 before each experiment. The concentrations used for the calibration curve were 0, 1, 2, 5, 10 and 20 ppb. The isotope detected was ^{193}Ir. Readings were done in triplicate. Rhodium was added as an internal standard at a concentration of 10 ppb to all samples. At least, three independent replicates were performed for each complex. The amount of iridium was expressed in relation to the number of cells in each sample.

3.4 Internalization kinetics

To evaluate the internalization kinetics of the complexes, A549 cells were seeded in 12-well plates at a density of 100 000 cells per well. After 24 h, the cells were treated with **IrL1–IrL3** at 5 μM for 6 h, 4 h, 2 h, 1 h, 30 min and 10 min. Non-treated cells were used as a control. Subsequently, the cells were washed with PBS, trypsinized, centrifuged, and washed again with PBS. The fluorescence emission of the cells at a wavelength of 675 nm was measured using a Novocyte flow cytometer (Agilent Technologies) equipped with a blue laser. For each sample, the median fluorescence intensity of 10 000 cells was determined. Internalization kinetics were determined by fitting the measured data to one-phase exponential association curves using GraphPad Prism software. Three independent experiments were carried out.

3.5 Cytotoxic activity

The effects of **IrL1–IrL5** on cell viability were evaluated in all four cell lines. The cells were seeded in 96 well plates at varying densities: 2500 cells per well for A549, 2000 cells per well for HeLa, 3500 cells per well for PC-3, and 5500 cells per well for MRC-5, and allowed to attach for 24 hours. Cells were incubated for 4 h with the complexes diluted in cell culture medium at concentrations ranging from 50 to 0.01 μM, to allow their internalization. The plates were then subjected to photoactivation with blue light (460 nm) for 1 h (light dose: 24.1 J cm^{-2}) or maintained without light irradiation as dark controls. Subsequently, the cells were incubated in the dark for an additional 43 h. The cellular viability was evaluated using the 3-(4,5-dimethylthiazol-2-yl)-2,5-diphenyltetrazolium bromide MTT assay (Sigma). Briefly, plates were washed with PBS and an MTT solution at 0.5 mg mL^{-1} in cell culture medium was added to each well. Two hours later, the MTT solution was removed, and the purple formazan crystals were dissolved in DMSO (100 μL per well). The absorbance of each well was measured using a Multiscan Plate Reader (Synergy 4, Biotek, Winooski, USA) at a wavelength of 570 nm. The concentration that reduced cell viability by 50% (IC_{50}) was established for each complex using Gen5 software (BioTek). Three replicates were analysed for each condition, and at least three independent experiments were performed for each complex. Mean values are reported using two significant digits.

3.6 Haemolysis assay

The activity of the complexes against red blood cells (RBCs) was investigated by haemolysis assays. Commercial pig blood preserved with sodium polyphosphate as an anticoagulant was used for this study. The blood was diluted to a concentration of 5% with PBS and washed three times with PBS by centrifugation at 1000 rcf for 10 minutes. Subsequently, 150 μL of diluted blood was mixed with 150 μL of each complex diluted at the corresponding $IC_{50,light}$ value obtained in A549 cells. The samples were then either irradiated with blue light or kept in the dark for one hour in an orbital shaker. Subsequently, they were centrifuged at 3500 rcf for 10 minutes. 80 μL of the supernatant were transferred to a 96-well plate and diluted with the same volume of water. The negative control was prepared using PBS instead of complex dilution, and the positive control was prepared using PBS with 0.2% Tween. The absor-

bance of each well was measured at 540 nm using a Synergy 4 plate reader (Biotek). The percentage of haemolysis (H (%)) was calculated using the following formula:

$$H\% = 100 \times \frac{(A_x - A_n)}{(A_p - A_n)}$$

where A_x is the absorption of the sample, A_n is the absorption of the negative control, and A_p is the absorption of the positive control.

3.7 Clonogeny assay

HeLa cells were seeded at a density of 100 000 cells per well in 12 well plates. After 24 h, the cells were incubated with **IrL1–IrL5** at the corresponding $IC_{50,light}$ for 4 h, and then either photoactivated with blue light (light dose: 24.1 J cm^{-2}) or kept in the dark for one hour. Treatment with cisplatin (Accord Healthcare) at the IC_{50} (1.5 μM) was used as a positive control. Untreated cells were used as a negative control. The cells were immediately harvested by trypsinization and counted using a Novocyte flow cytometer. Immediately, one thousand cells were seeded in 5 cm diameter cell culture dishes (Sarstedt) and incubated for 7 days to allow colony formation. The colonies were fixed and stained with 1% methylene blue in 70% ethanol and counted using an Alpha Innotech Imaging System (Alpha Innotech) and Fiji ImageJ software. Each compound was analysed in triplicate.

3.8 Confocal microscopy

The cellular localization of the complexes was assessed by confocal fluorescence microscopy. A549 cells were seeded onto glass-bottomed 8-well chamber slides (Ibidi) at a density of 50 000 cells per well. After 24 h, the cells were treated with **IrL1** diluted at 25 μM in DMEM or with DMEM alone as a negative control. The specific dyes MitoView™ Green (Biotium) and LysoTracker™ Green DND-26 (Thermo Fisher Scientific) at 100 nM were used to analyse co-localization with mitochondria and lysosomes, respectively. The cells were incubated for 1 h at 37 °C. Subsequently, the medium was removed, and the cells were washed with cold PBS. Confocal fluorescence microscopy images were immediately taken using a Nikon A1R microscope and analysed with an NIS-Elements AR (Nikon, Japan) and Fiji ImageJ software. The JACoP plugin was used to calculate the Pearson's co-localization coefficient.[68]

3.9 Mitochondrial damage

The effect on the mitochondrial function was assessed by confocal microscopy using the MitoTracker™ Red CMXRos dye (ThermoFisher Scientific). A549 cells were seeded on glass-bottom slide chambers at a density of 50 000 cells per well, treated with **IrL5** at the corresponding $IC_{50,light}$ for 4 h and then irradiated with blue light for one hour or kept in the dark. Untreated cells were used as the negative control. Subsequently, the cells were washed 3 times with PBS and incubated with MitoTracker™ Red CMXRos (Molecular Probes) at 200 nM in DMEM for 30 minutes at 37 °C. Cell nuclei were counterstained in blue with Hoechst 33342 (Invitrogen) diluted at 1 : 4000 in DMEM without phenol red. Mitochondrial staining was evaluated by confocal microscopy using a Nikon A1R confocal microscope.

3.10 Statistics

Statistical analysis was performed using GraphPad Prism (GraphPad Software). Quantitative variables were expressed as mean or median and standard deviation (SD). Statistical differences were analysed by the Mann–Whitney non-parametric test. A p-value < 0.05 was considered statistically significant.

Conclusions

A new family of five Ir(III) complexes bearing two units of a common C^N ligand derived from 1-phenyl-β-carboline and one unit of a bipyridine based N^N ligand have been prepared and studied to evaluate their potential use as anticancer PDT agents. Thus, increasing the number of aromatic rings in the ancillary ligand has been shown to broaden the absorption band in the visible region, especially for **IrL4** and **IrL5**. Besides, it was observed that the intensity of the emission band is reduced, and λ_{em} is slightly shifted when the aromaticity is increased. The presence of **L4** and **L5** in the PSs leads to the formation of self-aggregates at high concentrations, but these processes are negligible at low concentrations.

Regarding their biological properties, all our complexes feature cytotoxic activity against different cancer cells with IC_{50} values in the low micromolar range in the absence of light irradiation, reaching sub-micromolar values upon photoirradiation with blue light in many cases. This leads to moderate PIs for **IrL1–IrL4** and remarkable PIs for **IrL5** in the different cancer cells (PI = 15–38). Besides, it has been shown that all our complexes can internalize within cancer cells, though they display very different cellular uptake values. Notably, **IrL2** and **IrL3** exhibited significantly higher intracellular accumulation relative to **IrL1**, and particularly when compared to **IrL4** and **IrL5**. Moreover, these PSs accumulate preferentially within mitochondria as seen by confocal microscopy for the emissive complex **IrL1**.

On the other hand, the prominent photodynamic behavior of **IrL5** can be rationalized as a result of its prolonged excited state lifetime (4130 ns), its excellent ability to generate $^1O_2$ ($\Phi_\Delta \sim 1$) and its outstanding capacity to photo-catalyse the oxidation of the mitochondrial co-factor NADH, which correlates well with its ability to cause mitochondrial membrane depolarization. The results of this work could be used for the design of future photosensitizers. Moreover, conjugation to carrier proteins and encapsulation studies are planned in our laboratories to improve the cellular uptake of **IrL5**.

Author contributions

Juan Sanz-Villafruela: conceptualization, investigation, methodology, writing – original draft, and formal analysis; Cristina

Bermejo-Casadesus: investigation, formal analysis, methodology, and visualization; Marta Martínez-Alonso: investigation and methodology; Artur Moro: investigation; João C. Lima: resources and project administration; Anna Massaguer: investigation, methodology, validation, funding acquisition, supervision, writing – original draft, and project administration; Gustavo Espino: conceptualization, funding acquisition, methodology, supervision, writing – original draft, and project administration.

Conflicts of interest

There are no conflicts to declare.

Acknowledgements

This work was supported by the MCIN/AEI of Spain (projects PID2021-127187OB-C21 and PID2021-127187OB-C22). The PhD students acknowledge their predoctoral grants to Universidad de Burgos (J. S. V., 2019/00002/008/001) and University of Girona (C. B., IFUdG 2021).

References

1 D. Luo, K. A. Carter, D. Miranda and J. F. Lovell, Chemophototherapy: An Emerging Treatment Option for Solid Tumors, *Adv. Sci.*, 2017, **4**, 1600106.
2 C. Reichardt, S. Monro, F. H. Sobotta, K. L. Colón, T. Sainuddin, M. Stephenson, E. Sampson, J. Roque, H. Yin, J. C. Brendel, C. G. Cameron, S. McFarland and B. Dietzek, Predictive Strength of Photophysical Measurements for in Vitro Photobiological Activity in a Series of Ru(II) Polypyridyl Complexes Derived from π-Extended Ligands, *Inorg. Chem.*, 2019, **58**, 3156–3166.
3 J.-Y. Zhou, Q.-H. Shen, X.-J. Hong, W.-Y. Zhang, Q. Su, W.-G. Li, B. Cheng, C.-P. Tan and T. Wu, Synergization of an endoplasmic reticulum-targeted iridium(III) photosensitizer with PD-L1 inhibitor for oral squamous cell carcinoma immunotherapy, *Chem. Eng. J.*, 2023, **474**, 145516.
4 H. Yin, M. Stephenson, J. Gibson, E. Sampson, G. Shi, T. Sainuddin, S. Monro and S. A. McFarland, In Vitro Multiwavelength PDT with 3 IL States: Teaching Old Molecules New Tricks, *Inorg. Chem.*, 2014, **53**, 4548–4559.
5 E. S. Nyman and P. H. Hynninen, Research advances in the use of tetrapyrrolic photosensitizers for photodynamic therapy, *J. Photochem. Photobiol., B*, 2004, **73**, 1–28.
6 M. Li, Y. Xu, Z. Pu, T. Xiong, H. Huang, S. Long, S. Son, L. Yu, N. Singh, Y. Tong, J. L. Sessler, X. Peng and J. S. Kim, Photoredox catalysis may be a general mechanism in photodynamic therapy, *Proc. Natl. Acad. Sci. U. S. A.*, 2022, **119**, 1–8.
7 T. J. Dougherty, C. J. Gomer, B. W. Henderson, G. Jori, D. Kessel, M. Korbelik, J. Moan and Q. Peng, Photodynamic Therapy, *J. Natl. Cancer Inst.*, 1998, **91**, 889–905.
8 D. E. J. G. J. Dolmans, D. Fukumura and R. K. Jain, TIMELINE: Photodynamic therapy for cancer, *Nat. Rev. Cancer*, 2003, **3**, 380–387.
9 M. Martínez-Alonso, N. Busto, L. D. Aguirre, L. Berlanga, M. C. Carrión, J. V. Cuevas, A. M. Rodríguez, A. Carbayo, B. R. Manzano, E. Ortí, F. A. Jalón, B. García and G. Espino, Strong Influence of the Ancillary Ligand over the Photodynamic Anticancer Properties of Neutral Biscyclometalated Ir III Complexes Bearing 2-Benzoazole-Phenolates, *Chem. – Eur. J.*, 2018, **24**, 17523–17537.
10 X. Li, S. Kolemen, J. Yoon and E. U. Akkaya, Activatable Photosensitizers: Agents for Selective Photodynamic Therapy, *Adv. Funct. Mater.*, 2017, **27**, 1604053.
11 L. Zhang and D. Ding, Recent advances of transition Ir(III) complexes as photosensitizers for improved photodynamic therapy, *View*, 2021, **2**, 20200179.
12 A. Zamora, G. Vigueras, V. Rodríguez, M. D. Santana and J. Ruiz, Cyclometalated iridium(III) luminescent complexes in therapy and phototherapy, *Coord. Chem. Rev.*, 2018, **360**, 34–76.
13 J. Shen, T. W. Rees, L. Ji and H. Chao, Recent advances in ruthenium(II) and iridium(III) complexes containing nanosystems for cancer treatment and bioimaging, *Coord. Chem. Rev.*, 2021, **443**, 214016.
14 X. Jiang, N. Zhu, D. Zhao and Y. Ma, New cyclometalated transition-metal based photosensitizers for singlet oxygen generation and photodynamic therapy, *Sci. China: Chem.*, 2016, **59**, 40–52.
15 D. Ma, S. Lin, W. Wang, C. Yang and C. Leung, Luminescent chemosensors by using cyclometalated iridium(III) complexes and their applications, *Chem. Sci.*, 2016, **7**, 1–812.
16 C. Fan and C. Yang, Yellow/orange emissive heavy-metal complexes as phosphors in monochromatic and white organic light-emitting devices, *Chem. Soc. Rev.*, 2014, **43**, 6439–6469.
17 P. Cantero-López, D. Páez-Hernández and R. Arratia-Pérez, The origin of phosphorescence in Iridium(III) complexes. The role of relativistic effects, *Chem. Phys. Lett.*, 2017, **685**, 60–68.
18 S. P. Y. Li, C. T. S. Lau, M. W. Louie, Y. W. Lam, S. H. Cheng and K. K. W. Lo, Mitochondria-targeting cyclometalated iridium(III)-PEG complexes with tunable photodynamic activity, *Biomaterials*, 2013, **34**, 7519–7532.
19 L. C.-C. Lee and K. K.-W. Lo, Luminescent and Photofunctional Transition Metal Complexes: From Molecular Design to Diagnostic and Therapeutic Applications, *J. Am. Chem. Soc.*, 2022, **144**, 14420–14440.
20 J. S. Nam, M.-G. Kang, J. Kang, S.-Y. Park, S. J. C. Lee, H.-T. Kim, J. K. Seo, O.-H. Kwon, M. H. Lim, H.-W. Rhee and T.-H. Kwon, Endoplasmic Reticulum-Localized Iridium (III) Complexes as Efficient Photodynamic Therapy Agents via Protein Modifications, *J. Am. Chem. Soc.*, 2016, **138**, 10968–10977.

21 B. A. Albani, B. Peña, N. A. Leed, N. A. B. G. De Paula, C. Pavani, M. S. Baptista, K. R. Dunbar and C. Turro, Marked improvement in photoinduced cell death by a new tris-heteroleptic complex with dual action: Singlet oxygen sensitization and ligand dissociation, *J. Am. Chem. Soc.*, 2014, **136**, 17095–17101.

22 Y. Sun, L. E. Joyce, N. M. Dickson and C. Turro, Efficient DNA photocleavage by $[Ru(bpy)_2(dppn)]^{2+}$ with visible light, *Chem. Commun.*, 2010, **46**, 2426.

23 Y. Wang, Y. Wang and Y. Gu, in *Efficient photodynamic therapy against Staphylococcus aureus using [Ru(bpy)$_2$(dppn)]$^{2+}$: a novel cationic photosensitizer*, ed. Q. Luo, Y. Gu and X. D. Li, 2012, pp. 85530H.

24 W. Lei, Q. Zhou, G. Jiang, B. Zhang and X. Wang, Photodynamic inactivation of Escherichia coli by Ru(II) complexes, *Photochem. Photobiol. Sci.*, 2011, **10**, 887–890.

25 K. K. Lo, C. Chung and N. Zhu, Nucleic Acid Intercalators and Avidin Probes Derived from Luminescent Cyclometalated Iridium(III)–Dipyridoquinoxaline and –Dipyridophenazine Complexes, *Chem. – Eur. J.*, 2006, **12**, 1500–1512.

26 J.-J. Cao, Y. Zheng, X.-W. Wu, C.-P. Tan, M.-H. Chen, N. Wu, L.-N. Ji and Z.-W. Mao, Anticancer Cyclometalated Iridium(III) Complexes with Planar Ligands: Mitochondrial DNA Damage and Metabolism Disturbance, *J. Med. Chem.*, 2019, **62**, 3311–3322.

27 N. Busto, G. Vigueras, N. Cutillas, B. García and J. Ruiz, Inert cationic iridium(III) complexes with phenanthroline-based ligands: application in antimicrobial inactivation of multidrug-resistant bacterial strains, *Dalton Trans.*, 2022, **51**, 9653–9663.

28 J. Kasparkova, A. Hernández-García, H. Kostrhunova, M. Goicuría, V. Novohradsky, D. Bautista, L. Markova, M. D. Santana, V. Brabec and J. Ruiz, Novel 2-(5-Arylthiophen-2-yl)-benzoazole Cyclometalated Iridium(III) dppz Complexes Exhibit Selective Phototoxicity in Cancer Cells by Lysosomal Damage and Oncosis, *J. Med. Chem.*, 2024, **67**, 691–708.

29 Z. Molphy, A. Prisecaru, C. Slator, N. Barron, M. McCann, J. Colleran, D. Chandran, N. Gathergood and A. Kellett, Copper Phenanthrene Oxidative Chemical Nucleases, *Inorg. Chem.*, 2014, **53**, 5392–5404.

30 F. Hadjaz, S. Yous, N. Lebegue, P. Berthelot and P. Carato, A mild and efficient route to 2-benzyl tryptamine derivatives via ring-opening of β-carbolines, *Tetrahedron*, 2008, **64**, 10004–10008.

31 S. Rajkumar, S. Karthik and T. Gandhi, Ru(II)-Catalyzed β-Carboline Directed C–H Arylation and Isolation of Its Cycloruthenated Intermediates, *J. Org. Chem.*, 2015, **80**, 5532–5545.

32 M. Nonoyama, Benzo[h]quinolin-10-yl-N Iridium(III) Complexes, *Bull. Chem. Soc. Jpn.*, 1974, **47**, 767–768.

33 M. Nonoyama, Chelating C-metallation of N-phenylpyrazole with rhodium(III) and iridium(III), *J. Organomet. Chem.*, 1975, **86**, 263–267.

34 C. Pérez-Arnaiz, M. I. Acuña, N. Busto, I. Echevarría, M. Martínez-Alonso, G. Espino, B. García and F. Domínguez, Thiabendazole-based Rh(III) and Ir(III) bis-cyclometallated complexes with mitochondria-targeted anticancer activity and metal-sensitive photodynamic activity, *Eur. J. Med. Chem.*, 2018, **157**, 279–293.

35 N. A. Aksenov, N. A. Arutiunov, A. V. Aksenov, I. V. Aksenova, E. V. Aleksandrova, D. A. Aksenov and M. Rubin, Nitrovinylindoles as Heterotrienes: Electrocyclic Cyclization En Route to β-Carbolines: Total Synthesis of Alkaloids Norharmane, Harmane, and Eudistomin N, *Org. Lett.*, 2022, **24**, 7062–7066.

36 B. Orwat, E. Witkowska, I. Kownacki, M.-J. Oh, M. Hoffmann, M. Kubicki, I. Grzelak, B. Marciniec, I. Glowacki, B. Luszczynska, G. Wiosna-Salyga, J. Ulanski, P. Ledwon and M. Lapkowski, Microwave-assisted one-pot synthesis of new ionic iridium complexes of [Ir(bzq)2(N^N)]+ A − type and their selected electroluminescent properties, *Dalton Trans.*, 2017, **46**, 9210–9226.

37 L. He, L. Duan, J. Qiao, R. Wang, P. Wei, L. Wang and Y. Qiu, Blue–Emitting Cationic Iridium Complexes with 2-(1H-Pyrazol-1-yl)pyridine as the Ancillary Ligand for Efficient Light–Emitting Electrochemical Cells, *Adv. Funct. Mater.*, 2008, **18**, 2123–2131.

38 P. Pla, J. M. Junquera-Hernández, H. J. Bolink and E. Ortí, Emission energy of azole-based ionic iridium(III) complexes: a theoretical study, *Dalton Trans.*, 2015, **44**, 8497–8505.

39 P. Dreyse, M. Santander-Nelli, D. Zambrano, L. Rosales and L. Sanhueza, Electron–donor substituents on the dppz–based ligands to control luminescence from dark to bright emissive state in Ir(III) complexes, *Int. J. Quantum Chem.*, 2020, **120**, 1–14.

40 L. Wang, P. Cui, L. Lystrom, J. Lu, S. Kilina and W. Sun, Heteroleptic cationic iridium(III) complexes bearing phenanthroline derivatives with extended π-conjugation as potential broadband reverse saturable absorbers, *New J. Chem.*, 2020, **44**, 456–465.

41 W. He, D. Zu, D. Liu and R. Cheng, A series of iridium complexes equipped with inert shields: Highly efficient bluish green emitters with reduced self-quenching effect in solid state, *Inorg. Chim. Acta*, 2011, **365**, 78–84.

42 J. H. Kang, H. J. Kim, T.-H. Kwon and J.-I. Hong, Phosphorescent sensor for phosphorylated peptides based on an iridium complex, *J. Org. Chem.*, 2014, **79**, 6000–6005.

43 B. Tong, H. Wang, M. Chen, S. Zhou, Y. Hu, Q. Zhang, G. He, L. Fu, H. Shi, L. Jin and H. Zhou, High efficiency green OLEDs based on homoleptic iridium complexes with steric phenylpyridazine ligands, *Dalton Trans.*, 2018, **47**, 12243–12252.

44 J.-J. Cao, Y. Zheng, X.-W. Wu, C.-P. Tan, M.-H. Chen, N. Wu, L.-N. Ji and Z.-W. Mao, Anticancer Cyclometalated Iridium(III) Complexes with Planar Ligands: Mitochondrial DNA Damage and Metabolism Disturbance, *J. Med. Chem.*, 2019, **62**, 3311–3322.

45 V. Novohradsky, G. Vigueras, J. Pracharova, N. Cutillas, C. Janiak, H. Kostrhunova, V. Brabec, J. Ruiz and J. Kasparkova, Molecular superoxide radical photogenera-

tion in cancer cells by dipyridophenazine iridium(III) complexes, *Inorg. Chem. Front.*, 2019, **6**, 2500–2513.

46 R. D. Costa, E. Ortí, H. J. Bolink, F. Monti, G. Accorsi, N. Armaroli, E. Orti, H. J. Bolink, F. Monti, G. Accorsi and N. Armaroli, Luminescent ionic transition-metal complexes for light-emitting electrochemical cells, *Angew. Chem., Int. Ed.*, 2012, **51**, 8178–8211.

47 E. Ishow and A. Gourdon, Observation of supramolecular π–π dimerization of a dinuclear ruthenium complex by ^{1}H NMR and ESMS, *Chem. Commun.*, 1998, 1909–1910.

48 N. P. Toupin, S. Nadella, S. J. Steinke, C. Turro and J. J. Kodanko, Dual-Action Ru(II) Complexes with Bulky π-Expansive Ligands: Phototoxicity without DNA Intercalation, *Inorg. Chem.*, 2020, **59**, 3919–3933.

49 W. Chen, M. Qiu, R. Tu, X. Mu, F. Fu and M.-J. Li, Aggregation-Induced Near-Infrared Emission and Electrochemiluminescence of an Iridium(III) Complex for Ampicillin Sodium Sensing, *Inorg. Chem.*, 2023, **62**, 11708–11717.

50 A. S. Shetty, J. Zhang and J. S. Moore, Aromatic π-Stacking in Solution as Revealed through the Aggregation of Phenylacetylene Macrocycles, *J. Am. Chem. Soc.*, 1996, **118**, 1019–1027.

51 S. D. Bergman and M. Kol, π-Stacking Induced NMR Spectrum Splitting in Enantiomerically Enriched Ru(II) Complexes: Evaluation of Enantiomeric Excess, *Inorg. Chem.*, 2005, **44**, 1647–1654.

52 D. M. Arias-Rotondo and J. K. McCusker, The photophysics of photoredox catalysis: a roadmap for catalyst design, *Chem. Soc. Rev.*, 2016, **45**, 5803–5820.

53 T. Entradas, S. Waldron and M. Volk, The detection sensitivity of commonly used singlet oxygen probes in aqueous environments, *J. Photochem. Photobiol., B*, 2020, **204**, 111787.

54 S. Dadwal, H. Deol, M. Kumar and V. Bhalla, AIEE Active Nanoassemblies of Pyrazine Based Organic Photosensitizers as Efficient Metal-Free Supramolecular Photoredox Catalytic Systems, *Sci. Rep.*, 2019, **9**, 11142.

55 R. W. Redmond and J. N. Gamlin, A Compilation of Singlet Oxygen Yields from Biologically Relevant Molecules, *Photochem. Photobiol.*, 1999, **70**, 391–475.

56 H. Huang, S. Banerjee, K. Qiu, P. Zhang, O. Blacque, T. Malcomson, M. J. Paterson, G. J. Clarkson, M. Staniforth, V. G. Stavros, G. Gasser, H. Chao and P. J. Sadler, Targeted photoredox catalysis in cancer cells, *Nat. Chem.*, 2019, **11**, 1041–1048.

57 C. Huang, C. Liang, T. Sadhukhan, S. Banerjee, Z. Fan, T. Li, Z. Zhu, P. Zhang, K. Raghavachari and H. Huang, In–vitro and In–vivo Photocatalytic Cancer Therapy with Biocompatible Iridium(III) Photocatalysts, *Angew. Chem., Int. Ed.*, 2021, **60**, 9474–9479.

58 X.-Q. Zhou, M. Xiao, V. Ramu, J. Hilgendorf, X. Li, P. Papadopoulou, M. A. Siegler, A. Kros, W. Sun and S. Bonnet, The Self-Assembly of a Cyclometalated Palladium Photosensitizer into Protein-Stabilized Nanorods Triggers Drug Uptake In Vitro and In Vivo, *J. Am. Chem. Soc.*, 2020, **142**, 10383–10399.

59 L. D. Zorova, V. A. Popkov, E. Y. Plotnikov, D. N. Silachev, I. B. Pevzner, S. S. Jankauskas, V. A. Babenko, S. D. Zorov, A. V. Balakireva, M. Juhaszova, S. J. Sollott and D. B. Zorov, Mitochondrial membrane potential, *Anal. Biochem.*, 2018, **552**, 50–59.

60 J. Zielonka, J. Joseph, A. Sikora, M. Hardy, O. Ouari, J. Vasquez-Vivar, G. Cheng, M. Lopez and B. Kalyanaraman, Mitochondria-Targeted Triphenylphosphonium-Based Compounds: Syntheses, Mechanisms of Action, and Therapeutic and Diagnostic Applications, *Chem. Rev.*, 2017, **117**, 10043–10120.

61 W. W. Qin, Z. Y. Pan, D. H. Cai, Y. Li and L. He, Cyclometalated iridium(III) complexes for mitochondria-Targeted combined chemo-photodynamic therapy, *Dalton Trans.*, 2020, **49**, 3562–3569.

62 Y. Li, C.-P. Tan, W. Zhang, L. He, L.-N. Ji and Z.-W. Mao, Phosphorescent iridium(III)-bis-N-heterocyclic carbene complexes as mitochondria-targeted theranostic and photodynamic anticancer agents, *Biomaterials*, 2015, **39**, 95–104.

63 E. Zafon, I. Echevarría, S. Barrabés, B. R. Manzano, F. A. Jalón, A. M. Rodríguez, A. Massaguer and G. Espino, Photodynamic therapy with mitochondria-targeted biscyclometallated Ir(III) complexes. Multi-action mechanism and strong influence of the cyclometallating ligand, *Dalton Trans.*, 2022, **51**, 111–128.

64 I. Echevarría, E. Zafon, S. Barrabés, M.Á Martínez, S. Ramos-Gómez, N. Ortega, B. R. Manzano, F. A. Jalón, R. Quesada, G. Espino and A. Massaguer, Rational design of mitochondria targeted thiabendazole-based Ir(III) biscyclometalated complexes for a multimodal photodynamic therapy of cancer, *J. Inorg. Biochem.*, 2022, **231**, 111790.

65 E. Gambini, I. Martinelli, I. Stadiotti, M. C. Vinci, A. Scopece, L. Eramo, E. Sommariva, J. Resta, S. Benaouadi, E. Cogliati, A. Paolin, A. Parini, G. Pompilio and F. Savagner, Differences in Mitochondrial Membrane Potential Identify Distinct Populations of Human Cardiac Mesenchymal Progenitor Cells, *Int. J. Mol. Sci.*, 2020, **21**, 7467.

66 M. L. Coleman, E. A. Sahai, M. Yeo, M. Bosch, A. Dewar and M. F. Olson, Membrane blebbing during apoptosis results from caspase-mediated activation of ROCK I, *Nat. Cell Biol.*, 2001, **3**, 339–345.

67 G. R. Fulmer, A. J. M. Miller, N. H. Sherden, H. E. Gottlieb, A. Nudelman, B. M. Stoltz, J. E. Bercaw and K. I. Goldberg, *Organometallics*, 2010, **29**, 2176–2179.

68 S. Bolte and F. P. Cordelières, A guided tour into subcellular colocalization analysis in light microscopy, *J. Microsc.*, 2006, **224**, 213–232.